

REPORT DOCUMENTATION PAGEForm Approved
OMB No. 0704-0188

Public reporting burden for this collection of information is estimated to average 1 hour per response, including the time for reviewing instructions, searching existing data sources, gathering and maintaining the data needed, and completing and reviewing this collection of information. Send comments regarding this burden estimate or any other aspect of this collection of information, including suggestions for reducing this burden to Department of Defense, Washington Headquarters Services, Directorate for Information Operations and Reports (0704-0188), 1215 Jefferson Davis Highway, Suite 1204, Arlington, VA 22202-4302. Respondents should be aware that notwithstanding any other provision of law, no person shall be subject to any penalty for failing to comply with a collection of information if it does not display a currently valid OMB control number. **PLEASE DO NOT RETURN YOUR FORM TO THE ABOVE ADDRESS.**

1. REPORT DATE (DD-MM-YYYY)		2. REPORT TYPE Technical Papers		3. DATES COVERED (From - To)	
4. TITLE AND SUBTITLE				5a. CONTRACT NUMBER	
				5b. GRANT NUMBER	
				5c. PROGRAM ELEMENT NUMBER	
6. AUTHOR(S)				5d. PROJECT NUMBER 2303	
				5e. TASK NUMBER M2C8	
				5f. WORK UNIT NUMBER	
7. PERFORMING ORGANIZATION NAME(S) AND ADDRESS(ES) Air Force Research Laboratory (AFMC) AFRL/PRS 5 Pollux Drive Edwards AFB CA 93524-7048				8. PERFORMING ORGANIZATION REPORT	
9. SPONSORING / MONITORING AGENCY NAME(S) AND ADDRESS(ES) Air Force Research Laboratory (AFMC) AFRL/PRS 5 Pollux Drive Edwards AFB CA 93524-7048				10. SPONSOR/MONITOR'S ACRONYM(S)	
				11. SPONSOR/MONITOR'S NUMBER(S)	
12. DISTRIBUTION / AVAILABILITY STATEMENT Approved for public release; distribution unlimited.					
13. SUPPLEMENTARY NOTES					
14. ABSTRACT					
15. SUBJECT TERMS					
16. SECURITY CLASSIFICATION OF:			17. LIMITATION OF ABSTRACT A	18. NUMBER OF PAGES	19a. NAME OF RESPONSIBLE PERSON Leilani Richardson
a. REPORT Unclassified	b. ABSTRACT Unclassified	c. THIS PAGE Unclassified			19b. TELEPHONE NUMBER (include area code) (661) 275-5015

Standard Form 298 (Rev. 8-98)
Prescribed by ANSI Std. Z39.18

62

separate items are enclosed

MEMORANDUM FOR PR (Contractor/In-House Publication)

FROM: PROI (TI) (STINFO)

15 May 2000

SUBJECT: Authorization for Release of Technical Information, Control Number: **AFRL-PR-ED-TP-2000-114**
Tam, S.; Macler, M. (HP); DeRose, M., Fajardo, M., "Electronic Spectroscopy of B Atoms and B₂
Molecules Isolated in para-H₂, normal-D₂, Ne, Ar, Kr, and Xe Matrices"

Journal of Chemical Physics

(Submission Deadline: 01 Jun 00)

(Statement A)

1. This request has been reviewed by the Foreign Disclosure Office for: a.) appropriateness of distribution statement, b.) military/national critical technology, c.) export controls or distribution restrictions, d.) appropriateness for release to a foreign nation, and e.) technical sensitivity and/or economic sensitivity.

Comments: _____

Signature _____ Date _____

2. This request has been reviewed by the Public Affairs Office for: a.) appropriateness for public release and/or b) possible higher headquarters review.

Comments: _____

Signature _____ Date _____

3. This request has been reviewed by the STINFO for: a.) changes if approved as amended, b.) appropriateness of distribution statement, c.) military/national critical technology, d.) economic sensitivity, e.) parallel review completed if required, and f.) format and completion of meeting clearance form if required

Comments: _____

Signature _____ Date _____

4. This request has been reviewed by PR for: a.) technical accuracy, b.) appropriateness for audience, c.) appropriateness of distribution statement, d.) technical sensitivity and economic sensitivity, e.) military/national critical technology, and f.) data rights and patentability

Comments: _____

APPROVED/APPROVED AS AMENDED/DISAPPROVED

ROBERT C. CORLEY
Senior Scientist (Propulsion)
Propulsion Directorate

(Date)

**Electronic Spectroscopy of B Atoms and B₂ Molecules Isolated in
para-H₂, normal-D₂, Ne, Ar, Kr, and Xe Matrices**

Simon Tam, Michel Macler,[†] Michelle E. DeRose, and Mario E. Fajardo^{*}
U.S. Air Force Research Laboratory, Propulsion Directorate
AFRL/PRSP, Bldg. 8451, Edwards AFB, CA 93524-7680

^{*} email: mario_fajardo@ple.af.mil

[†] present address: Hewlett-Packard Co., 1000 NE Circle Blvd., Corvallis, OR 97330-4239

Submitted to J. Chem. Phys. _____, Received _____, Accepted _____

ABSTRACT

We report spectroscopic observations on B atoms isolated in cryogenic parahydrogen (pH₂), normal deuterium (nD₂), Ne, Ar, Kr, and Xe matrices, and of B₂ molecules in Ne, Ar, Kr, and Xe matrices. The 2s²3s(²S) ← 2s²2p(²P) B atom Rydberg absorption suffers large gas-to-matrix blue shifts, increasing from +3000 to +7000 cm⁻¹ in the host sequence: Xe < Kr < Ar ≈ Ne ≈ nD₂ ≈ pH₂. Much smaller shifts are observed for the 2s2p²(²D) ← 2s²2p(²P) B atom core-to-valence transition. We assign pairs of absorption peaks spaced by ≈ 10 nm in the 315 to 355 (nm) region to the B₂ (A ³Σ_u⁻ ← X ³Σ_g⁻) Douglas-Herzberg transition. We assign a much weaker progression in the 260 to 300 nm region to the B₂ (2) ³Π_u ← X ³Σ_g⁻ transition. We report a novel progression of strong peaks in the 180 to 200 nm region which we suspect may be due to B₂ molecules, but which remains unassigned. Ultraviolet (UV) absorption spectra of B/pH₂ solids show two strong peaks at 216.6 and 208.9 nm, which we assign to the matrix perturbed 2s²3s(²S) ← 2s²2p(²P) and 2s2p²(²D) ← 2s²2p(²P) B atom absorptions, respectively. This assignment is supported by quantum path integral simulations of B/pH₂ solids reported in the following article in this journal [J.R. Krumrine, S. Jang, G.A. Voth, and M.H. Alexander, J. Chem. Phys. XXX, yyyy (zzzz)]. Laser induced fluorescence emission spectra of B/pH₂ solids show a single line at 249.6 nm, coincident with the gas phase wavelength of the 2s²3s(²S) → 2s²2p(²P) B atom emission. The UV laser irradiation results in photobleaching of the B atom emission and absorptions, accompanied by the formation of B₂H₆.

try to
keep w/ #
on previous
line

20021122 008

Distribution A: Approved for public release, distribution unlimited.

I. Introduction

There are surprisingly few reports on the electronic spectroscopy of B atoms and B₂ molecules in the matrix isolation spectroscopy (MIS) literature.^{1,2} In fact, we find only three manuscripts which include ultraviolet (UV) absorption spectra of B and B₂, and these studies were performed exclusively in Ar matrices.³⁻⁵ Technical difficulties in evaporating elemental boron cannot completely explain this situation, as there are several groups actively pursuing electron spin resonance (ESR),⁶⁻¹³ infrared (IR) absorption,¹⁴⁻²³ and electronic²⁴⁻²⁷ spectroscopic studies on matrix isolated molecules containing B atoms. Rather, we believe that complementary experimental and theoretical results, essential to expanding upon the original understanding³ of the B/Ar and B₂/Ar matrix spectra, have only recently become available (*vide infra*).

Our work on trapping B atoms and small B_n clusters in cryogenic matrices is performed under the auspices of the U.S. Air Force's High Energy Density Matter (HEDM) Program.²⁸ Our ultimate goal is to incorporate large (~ 5 mol %) concentrations of these species as energetic additives in Cryogenic Solid Propellants.²⁹⁻³¹ The payoff for success could be a revolutionary improvement in the performance of chemical rocket propellants. Thermochemical calculations predict that a fuel consisting of 5 mol % B atoms in solid hydrogen, when combusted with liquid oxygen would deliver a ~ 20 % improvement in specific impulse³² (I_{sp}) over the state of the art liquid oxygen/liquid hydrogen propellant system.³³ I_{sp} is a measure of the momentum transferred to the rocket vehicle per mass of expended propellant, and is proportional to the mean velocity of the exhausted "working fluid."³² Since the propellant mass is a very large fraction of the mass of a fully loaded space launch vehicle,³⁴ a 20 % increase in I_{sp} can translate into a doubling or tripling of the system's payload capacity.

The data reported in this manuscript have been collected over a period of several years; our initial report of the UV absorption spectra of B atoms in normal hydrogen (nH₂) and normal deuterium (nD₂) matrices appeared in 1994.³⁵ Our improved comprehension of the spectroscopy of B atom doped cryogenic solids was made possible by experimental and theoretical results on the B-Ar,^{36,37} B-Ne,³⁸ and B-H₂³⁹⁻⁴⁶ interaction potentials, and on B/Ar⁴⁷⁻⁴⁹ and B/H₂^{50,51} clusters and solids. We note gratefully that these results have been obtained primarily by other HEDM Program participants. This support of our experimental effort culminates in the companion paper in this journal describing simulations of the UV absorption spectrum of B atoms isolated in solid

parahydrogen (pH_2).⁵² Independent of the HEDM program, pioneering studies of the photodynamics of Rydberg transitions of NO molecules trapped in solid hydrogen⁵³⁻⁵⁷ convinced us to accept the notion of very large (~ 1 eV) gas-to-matrix blue-shifts for B atom Rydberg transitions in solid pH_2 . Finally, our analysis of the matrix spectra also benefit from updated gas-phase spectroscopic observations⁵⁸⁻⁶² and quantum chemical calculations⁶³⁻⁶⁷ of the potential energy curves of the B_2 molecule.

In what follows we describe the various experimental apparatus used to produce and interrogate our B atom- and B_2 molecule-doped cryogenic solids. We will identify and assign (where possible) the observed spectra of B atoms in the different rare gas (Rg) matrix hosts; our new results require a revision to the original interpretation³ of the B/Ar UV absorption spectrum. We present new UV spectra of B_2 molecules in the various Rg matrices; including the well-known Douglas-Herzberg,⁵⁸ and another previously reported³ but unassigned B_2 absorption band. We also report a novel vibronic progression in the vacuum ultraviolet (VUV: $\lambda < 200$ nm) region in spectra of B/Rg matrices which we cannot assign. We show UV absorption, and laser induced fluorescence (LIF) emission spectra of B/ pH_2 solids which conclusively demonstrate the trapping of unreacted B atoms. We also observe photobleaching of the B atom absorptions in B/ pH_2 solids during UV irradiation, accompanied by the growth of the IR absorptions of B_2H_6 ; however, we defer a detailed discussion of the IR spectroscopy of these samples to a later time. A comparison of the direct UV absorption and photobleaching difference spectra provides the definitive absorption lineshape for comparison with the simulations in the companion paper. We conclude with a qualitative discussion of B atom photodynamics in B/ pH_2 solids.

II. Experimental

The spectra reported in this manuscript were recorded over several years of experimentation utilizing different and constantly evolving apparatus. Figure 1 shows schematic diagrams of the two canonical sample preparation geometries. The CLOSE geometry experiments are distinguished by having the laser ablation of a rotating solid boron target take place in the same vacuum chamber as the matrix deposition. The ablation target to deposition substrate distance is typically ≈ 3 cm. The deposition substrate (sapphire or BaF_2) has alternatively been cooled by: a 10 K closed-cycle He refrigerator (Ar, Kr, Xe hosts), a liquid helium (lHe) transfer cryostat (nD_2 , Ne hosts), and a lHe bath cryostat (pH_2 , nD_2/Ne , Ne hosts).

Our lHe bath cryostat provides a much lower base substrate temperature than the lHe transfer cryostat (2 K vs. 3.5 K), but it permits controlled annealing to only $T \approx 5$ K.

TASSPI is an acronym for "Temporally And Spatially Specific PhotoIonization," our technique for non-mechanical velocity selection of fast laser ablated metal atoms.⁶⁸⁻⁷² We have described matrix depositions using the TASSPI geometry in a manuscript on MIS of laser ablated carbon species.⁷³ The TASSPI geometry is distinguished by having the laser ablation process occur in a separate differentially pumped vacuum chamber; resulting in enhanced control over the ablation process as compared to ablation in the CLOSE geometry. First, by virtue of the differential pumping arrangement, we expect greatly reduced interactions between uncondensed matrix host gases and the laser ablated plume. Second, a pair of removable 2.5 cm diameter permanent magnets providing a ≈ 2 kG transverse magnetic field can be used to eliminate all but the fastest charged species from the ablated plume. These advantages come at the cost of greatly reduced delivered flux, due to the ≈ 20 cm separation between the ablation target and the deposition substrate.

We can tolerate this reduced dopant flux because of the millimeters-long absorption pathlengths enabled by the exceptional optical clarity of the pH₂ solids produced using our Rapid Vapor Deposition method.⁷⁴ We deposit pre-cooled pH₂ gas at flow rates ~ 100 mmol/hr, or about 100 times faster than typical for Rg host matrix depositions. The pH₂ is produced in our ortho/para (o/p) converter,⁷⁵ a catalyst-bed device consisting of an 1/8 inch outside diameter by 1.5 m long soft copper tube packed with 1.4 g of APACHI catalyst.⁷⁶ This tubing is wound onto an oxygen free high conductivity copper bobbin and potted in place with high thermal conductivity epoxy; a dedicated closed-cycle He refrigerator cools the bobbin. Operating the o/p converter at 15 K yields a flow of pre-cooled pH₂ gas with a residual oH₂ concentration ~ 0.01 %; this gas is delivered to the deposition substrate through a thin wall brass tube which impinges upon the substrate at a 45° angle. Individual sample preparation details are given in each figure caption.

We obtain VUV, UV, and IR absorption spectra, and LIF emission spectra, along the main optical axis depicted in Figure 1. For the VUV and UV absorption spectra, we employ an optical multichannel analyzer (OMA) consisting of an f/3.8, 275 mm focal length polychromator equipped with a variety of diffraction gratings, and either an intensified or an unintensified silicon diode array detector. The various combinations of these components yield different

try to
keep it #
on
previous
line

useable VUV cutoffs, explaining the inconsistent terminations of the absorption traces in the figures below. Because of day-to-day variations in the dry N₂ purge gas pressure inside the polychromator, and because of the limited spectral resolution and wavelength precision permitted by our apparatus, we calibrate all the spectra to the vacuum wavelengths of the Hg lamp calibration lines. We apply a cubic polynomial fit of wavelength vs. pixel element to account for all nonlinearities (including the dispersion in the index of refraction of the N₂ purge gas) in the optical system in one step. We estimate the resulting absolute wavelength errors to be less than +/- one pixel element, which translates to about +/- 0.1 nm for the 0.3 nm resolution spectra, and +/- 0.4 nm for the 1.2 nm resolution spectra presented below.

We determine the thickness of the Rg matrices during the deposition process by back-reflection interferometry using a HeNe laser and a DC coupled photodiode detector. For the much thicker pH₂ solids, we determine the thickness from the intensities of the condensed-phase induced IR absorptions of the pH₂ molecules themselves.

We use an excimer pumped dye laser system equipped with a barium beta-borate doubling crystal as the excitation source in the LIF experiments; this particular crystal's shape limits us to wavelengths longer than ≈ 207 nm. Detection is accomplished using the OMA system described above equipped with a gated, intensified silicon diode array detector. IR absorption spectra are obtained using a Fourier Transform IR spectrometer equipped with a glowbar source, a KBr beamsplitter, and a liquid nitrogen cooled HgCdTe (MCT) detector; this spectrometer is capable of ≈ 0.1 cm⁻¹ FWHM resolution.

III. Results and Discussion

A. Ne, Ar, Kr, and Xe hosts

Figure 2 shows survey spectra of laser ablated boron species trapped in Ne, Ar, Kr, and Xe matrices. The B/Ar spectrum shown in trace (b) includes the previously reported B atom absorptions near 208 and 214 nm, and B₂ absorptions near 320 and 330 nm, and the observed but unassigned progression of very weak peaks in the 260 to 300 nm region;³⁻⁵ however, the strong peaks observed in the VUV region are novel. The spectra in Ne, Kr, and Xe hosts are all new; a comparison reveals a definite trend of increasing red shifts for most spectral features in the matrix host sequence Ne \rightarrow Ar \rightarrow Kr \rightarrow Xe, and immediately suggests a few extensions of the original B/Ar and B₂/Ar assignments. Most of the peaks in the 200 to 250 nm region are likely

due to B atom transitions (*vide infra*); peak positions are summarized in Table I, along with gas-phase B atom transition energies.⁷⁷ However, there appear to be complications due to secondary trapping sites and overlapping by portions of the VUV absorption band, particularly for the Xe spectrum; thus, some of the assignments are listed in the table as "tentative." The pairs of peaks spaced by ≈ 10 nm appearing in the 315 to 355 nm region are clearly due to the B₂ (A $^3\Sigma_u^- \leftarrow X$ $^3\Sigma_g^-$) Douglas-Herzberg transition; these results are summarized in Table II, along with the gas phase B₂ transition energies.⁵⁹

Table III is a collection of experimentally and theoretically derived spectroscopic constants for the ground $^3\Sigma_g^-$, and first few excited $^3\Sigma_u^-$ and $^3\Pi_u$ symmetry states of $^{11}\text{B}_2$. We direct the reader to figure 1 of reference [65] for a graphical summary of the associated potential energy curves. We note that the second electronic state of $^3\Pi_u$ symmetry is predicted to have a minimum near $R_e \approx 1.47$ Å and $T_e \approx 34500$ cm⁻¹, with a vibrational frequency near 1300 cm⁻¹. The shift in potential minimum separation of -0.12 Å relative to the $^3\Sigma_g^-$ ground state suggests non-negligible Franck-Condon factors for the first few vibrations of the upper electronic state, starting from $v = 0$ in the ground state.

Table IV gives a summary of the observed peak positions in Ne, Ar, and Kr matrices, along with our proposed assignment to the (2) $^3\Pi_u \leftarrow X$ $^3\Sigma_g^-$ transition which is based on the good agreement with the theoretical predictions for the (2) $^3\Pi_u$ state. We give values for $\Delta G_{v+1/2}$, but the large experimental uncertainties (≈ 30 cm⁻¹) preclude any analysis of the anharmonicity of the (2) $^3\Pi_u$ potential. We note that the matrix dependent shifts of the Douglas-Herzberg and (2) $^3\Pi_u \leftarrow X$ $^3\Sigma_g^-$ transitions are quite similar. We will report the results of dispersed LIF experiments on the (2) $^3\Pi_u \leftrightarrow X$ $^3\Sigma_g^-$ system in Ne matrices upon completion of our analysis.

Figure 3 shows absorption spectra in (a) Ne and (b) mixed nD₂/Ne matrices, along with (c) the Schumann-Runge absorptions of O₂ in laboratory air (which is included to illustrate the instrumental capabilities: the positions of the band heads all appear within ± 0.1 nm of the literature values for spectra obtained at a comparable resolution⁷⁸). Since the features in the VUV band exhibit a variable intensity relative to the B atom peaks in the 200 to 220 nm region, we can exclude B atoms as the carrier for the VUV band. Unfortunately, we were unable to perform any controlled annealing experiments on these samples to see if the complicated lineshapes in the VUV band could be attributed to ^{10}B - ^{11}B isotopomers, or to multiple trapping

sites or some other structural inhomogeneity. Table V includes the peak positions for the VUV band in Ne, Ar, and Kr hosts. The spacings between adjacent peaks average to $\approx 950 \text{ cm}^{-1}$, which does not exclude a transition to a higher lying excited electronic state of B_2 .

We typically encountered severe optical scattering losses in spectra of B/Kr and B/Xe matrices. The caption to figure 2 describes how we correct those survey spectra by subtraction of the wavelength dependent losses observed in undoped matrices. Due to this complication, we limited our annealing studies to boron doped Ne and Ar matrices. Figure 4 shows the effects of annealing on the B atom absorptions in a Ne matrix. The peak at 205.4 nm disappears upon warming to $T \approx 10 \text{ K}$, so we assign it to B atoms isolated in a secondary, less thermally stable, trapping site. The peaks at 207.4 and 215.4 nm appear to anneal away at comparable rates, which supports the contention that both are due to B atoms in the same trapping site.

Figure 5 shows the effects of annealing on the B_2 ($A^3\Sigma_u^- \leftarrow X^3\Sigma_g^-$) Douglas-Herzberg absorptions in a Ne matrix. The complicated structure in each absorption peak is due to a combination of ^{10}B - ^{11}B isotopic shifts and the existence of multiple trapping sites for the B_2 molecules. We note the qualitative similarities between lineshapes in as-deposited B/Ne samples for the Douglas-Herzberg and VUV bands. We are tempted to see this similarity as evidence that the VUV band is an absorption to a higher lying electronically excited state of B_2 . However, the absolute magnitudes of the splittings and linewidths differ by a factor of ≈ 6 , diluting the value of this comparison in assigning the carrier of the VUV band.

Figure 6 shows the effects of annealing on the VUV band and B atom absorptions in an Ar matrix. The peaks at 208.4 and 213.9 nm appear to anneal away at comparable rates. The inset shows that the integrated intensity of the 208.4 nm peak correlates very well with that of the 213.9 nm peak, regardless of sample preparation conditions or annealing history. We thus assign the two peaks to two different electronic transitions of B atoms in the same trapping site, contradicting the original assignment to a single electronic transition of B atoms in two different trapping sites.³ We assign the 213.9 and 208.4 nm peaks to the matrix perturbed $2s^23s(^2S) \leftarrow 2s^22p(^2P)$ and $2s2p^2(^2D) \leftarrow 2s^22p(^2P)$ B atom absorptions, respectively. The ratio of the gas phase absorption intensities of these transitions is about 1.5:1,⁷⁷ in reasonable agreement with the 1.25:1 ratio we calculate from the slope of the correlation plot in figure 6.

These assignments reflect our expectation that the $2s^23s(^2S) \leftarrow 2s^22p(^2P)$ B atom "Rydberg" absorption should experience a large gas-to-matrix blue shift by virtue of the change

in principal quantum number, and hence increased radial extent, of the B atom valence electron probability distribution. Increased overlap of this outermost electron with the surrounding closed-shell Rg perturbers should lead to strongly repulsive B*/Rg interactions at the internuclear separations sampled by the trapped ground state B atom. In this situation, application of the Franck-Condon principle results in a strong blue-shift for the "vertical" optical absorption. In contrast, the $2s^2 3s(^2S) \leftarrow 2s^2 2p(^2P)$ B atom transition involves the excitation of a "core" 2s electron into a partially occupied 2p valence orbital. In this case the radial extent of the B atom electron distribution does not increase significantly, so we would expect the B*/Rg and ground state B/Rg interactions to be qualitatively similar; vertical transitions between these "nested" potential energy surfaces should result in smaller gas-to-matrix shifts. The observed trend of decreasing gas-to-matrix blue shifts in the matrix host sequence $\text{Ne} \rightarrow \text{Ar} \rightarrow \text{Kr} \rightarrow \text{Xe}$ is thus consistent with the corresponding increase in the volume of a single substitutional vacancy.

Our previous attempt at testing this simple picture quantitatively, via Monte Carlo simulations of B/Ar absorption spectra, correctly predicts a single absorption peak for the matrix perturbed $2s^2 3s(^2S) \leftarrow 2s^2 2p(^2P)$ transition⁴⁷ (*i.e.* the matrix environment cannot break the Kramers degeneracy⁷⁹ of the 2S state). However, the largest calculated gas-to-matrix blue shift of $+2500 \text{ cm}^{-1}$, obtained for the B atom in a single substitutional site, badly underpredicts the experimentally observed $+6700 \text{ cm}^{-1}$ blue-shift. We believe this discrepancy is due to the inadequacy of our first order degenerate perturbation theory treatment^{80,81} of the excited B*/Ar interactions. The relevant B-Ar $^2\Sigma^+$ potential (correlating to the B $2s^2 3s(^2S) + \text{Ar} (^1S_0)$ asymptote) exhibits a complicated behavior which "reflects a subtle interplay between electron correlation and the polarization of the B-Ar charge distribution."³⁶ Specifically, the potential curve exhibits a global minimum near $R_{\text{B-Ar}} \approx 2.2 \text{ \AA}$ bound by $\approx 1100 \text{ cm}^{-1}$, a barrier near $R_{\text{B-Ar}} \approx 3.8 \text{ \AA}$ of $\approx 180 \text{ cm}^{-1}$, and a second minimum near $R_{\text{B-Ar}} \approx 7 \text{ \AA}$ with a $\sim 10 \text{ cm}^{-1}$ binding energy.³⁶ The barrier occurs very near the 3.76 \AA nearest neighbor separation in solid Ar. Hence for a B atom in a single substitutional site (twelve nearest neighbors) our model predicts a gas-to-matrix blue shift for the $2s^2 3s(^2S) \leftarrow 2s^2 2p(^2P)$ transition of $\approx 12 \times 180 \text{ cm}^{-1} = 2160 \text{ cm}^{-1}$ (the actual calculated value includes the effects of structural relaxation away from the ideal lattice).

It thus appears that simulating the absorption spectrum of the B/Ar matrix system will require a more sophisticated treatment of the excited B*/Ar interactions. A new theoretical formalism, capable of including the contributions from higher lying B*-Ar diatomic states as

well as the effects of many-body interactions within the Ar solid, is currently under development.⁸² Efforts are underway to apply this formalism to optical absorptions in Al/Ar clusters and solids, with promising preliminary results.⁸³ If successful, this approach will be applied to B/Ar system.

In contrast to B-Ar, the B-Ne $^2\Sigma^+$ potential correlating to the B $2s^23s(^2S) + Ne(^1S_0)$ asymptote shows a monotonically increasing repulsion with decreasing B-Ne separation, with only a hint of a flat "shelf" region.³⁸ For $R_{B-Ne} = 3.16 \text{ \AA}$ (the nearest neighbor separation in solid Ne) the repulsion amounts to $\approx 340 \text{ cm}^{-1}$ per B-Ne pair. In this case, for a B atom in a single substitutional site, our model predicts a gas-to-matrix blue shift for the $2s^23s(^2S) \leftarrow 2s^22p(^2P)$ transition of $\approx 12 \times 340 \text{ cm}^{-1} = 4080 \text{ cm}^{-1}$, in somewhat better agreement with the observed $+6390 \text{ cm}^{-1}$ shift. Similarly, the interaction potential correlating to the B $2s^23s(^2S) + p\text{H}_2(^1\Sigma_g^+)$ asymptote also shows a monotonically increasing repulsion with decreasing B- $p\text{H}_2$ separation.^{40,41} As demonstrated in the following companion manuscript,⁵² in this case a first-order degenerate perturbation theory treatment of the B*/ $p\text{H}_2$ excited state again suffices to correctly predict the approximate gas-to-matrix blue shift and linewidth of the matrix perturbed B atom $2s^23s(^2S) \leftarrow 2s^22p(^2P)$ transition.

B. $p\text{H}_2$ and $n\text{D}_2$ hosts

Figure 7 shows the effects of annealing on the B atom absorptions in a $n\text{D}_2$ matrix. We tentatively assign the unresolved peaks at 204 and 207 nm, and the shoulder at 214 nm, to the same B atom transitions observed in Rg solids. Due to problems with strong optical scattering by the matrix host, we have only performed a handful of boron depositions in thin (1 to 10 μm) $n\text{D}_2$ and $n\text{H}_2$ matrices, so we are unwilling to draw many definite conclusions from such a limited data set. However, with this caveat in mind, we do note the complete absence (to date) of the Douglas-Herzberg B_2 absorptions in $n\text{D}_2$ matrices, even in spectra of other samples (not shown) which span the entire 200 to 400 nm region. This is surprising, especially in light of a preliminary report of the observation of B_2 in solid $n\text{D}_2$ via ESR.⁸ Our B/ $n\text{D}_2$ matrices were produced using ablation and deposition conditions that result in strong B_2 absorptions in Rg matrices. Our observations raise the interesting possibility that B_2 molecules are either chemically unstable, or cannot be formed by recombination of B atoms, in hydrogen solids.

We recently reported the UV transmission spectrum of a 1 mm thick B/pH₂ sample produced using our rapid vapor deposition technique.⁷⁴ This spectrum shows a greatly improved signal:noise ratio over our initial effort.³⁵ Figure 8 shows absorption spectra of two B/pH₂ samples produced via rapid vapor deposition and laser ablation in the TASSPI geometry; for trace (a) the ion-rejection magnets are absent during deposition, for trace (b) they are present between the ablation target and deposition substrate. Both samples are slightly over 2 mm thick, yet are transparent through most of the UV region. Spectra of pure pH₂ solids deposited under these conditions do not show the sloping baseline in the 180 to 240 nm region apparent in these traces. This suggests that the increasing absorbance at shorter wavelengths is due to a real electronic absorption, and not to scattering by the matrix host. We assign the peaks at 216.6 and 208.9 nm to the matrix perturbed $2s^23s(^2S) \leftarrow 2s^22p(^2P)$ and $2s2p^2(^2D) \leftarrow 2s^22p(^2P)$ B atom absorptions, respectively. This assignment is based on comparison with the B/Rg spectra presented above, and on the theoretical simulations of the B/pH₂ $2s^23s(^2S) \leftarrow 2s^22p(^2P)$ absorption lineshape described in the companion manuscript.⁵² The ratio of integrated absorption intensities of the 208.9 and 216.6 nm peaks is about 1.4:1, in good agreement with the 1.5:1 ratio of literature values.⁷⁷

The observation that the B atom absorptions in trace (8a) are significantly larger than in trace (8b) shows that nascent laser ablated B⁺ ions are contributing to the final yield of B atoms isolated in the pH₂ solid. The process of ion deposition and subsequent neutralization to yield isolated atoms has been demonstrated previously for Ti⁺ and Na⁺ ions in Ar matrices.^{84,85} The closed-shell B⁺ ions are actually less reactive (for small impact parameter encounters) with H₂ molecules than are the B atomic radicals; the ion-molecule reaction exhibits a barrier of ≈ 25000 cm⁻¹,⁸⁶⁻⁸⁸ whereas the barrier to the B atom + H₂ reaction is calculated as ≈ 5000 cm⁻¹.^{42,45}

Figure 9 shows the LIF emission spectrum of a B/pH₂ sample excited at 217.0 nm; the emission centroid occurs near 249.6 nm and the linewidth is ≈ 280 cm⁻¹ FWHM. Aside from a ≈ 300 times weaker feature centered at 266 nm (≈ 600 cm⁻¹ FWHM), no other emissions are observed over the 240 to 360 nm region. We observe the exact same peak wavelength and lineshape for the main emission feature for excitation laser wavelengths throughout the 207 to 220 nm region. This single sharp emission feature coincident with the position of the gas-phase B atom resonance line is further evidence that the 208.9 and 216.6 nm absorptions are due to

sep w/
on
previous
or move #
to next line)

isolated B atoms. The negligible gas-to-matrix shift and narrow linewidth implies that the B atom experiences minimal interactions with the pH₂ host during the emission process.

We observe a strong decrease in the B atom emission intensity after just a few hundred excitation laser pulses; figure 10 depicts the accompanying photobleaching of the B/pH₂ absorptions. Trace (10c) shows the "photobleaching difference spectrum," which is cleanly compensated for the noticeable optical scattering losses observed in this particular matrix. Both the 208.9 and 216.6 nm peaks, and the sloping baseline in the 180 to 240 nm region, all decrease in intensity simultaneously, consistent with their all being due to the same species. In the gas-phase B-H₂ complex, optical excitation to the 2s²3s(²S) B atom state does not lead to chemical reaction,⁴¹ whereas excitation to the 2s2p(²D) B atom state leads to chemiluminescence from excited BH products.⁴⁴ Perhaps due to the large gas-to-matrix blue-shift of the 2s²3s(²S) ← 2s²2p(²P) transition, this distinction may no longer hold in the pH₂ solid. It is also conceivable that B atoms may be lost to photo-induced mobility and recombination. However, since none of the traces in figure 10 show any hint of the B₂ Douglas-Herzberg absorptions, it appears that if any B₂ molecules are formed by B atom recombination, then they do not survive in solid pH₂.

Figure 11 shows IR absorption spectra of the sample depicted in Figures 9 and 10, in the ν_{17} band region of B₂H₆. The three strong peaks at 1596.7, 1599.0, and 1601.1 cm⁻¹, all exhibit instrument limited linewidths of ≈ 0.1 cm⁻¹ FWHM. The relative integrated intensities of these peaks are 0.643:0.314:0.043, in good agreement with the 0.644:0.317:0.039 values predicted for ¹¹B₂H₆:¹⁰B¹¹BH₆:¹⁰B₂H₆ isotopomers present at natural isotopic abundance.⁸⁹ The observed shifts upon single and double ¹⁰B substitution of +2.3 and +4.4 cm⁻¹, respectively, are in excellent agreement with the gas phase values of +2.249 and +4.41 cm⁻¹.^{90,91}

We estimate the number densities of isolated B atoms, N_B, from the integrated observed atomic absorptions using the relationship⁹² (in SI units):

$$2.303 \int_{\text{band}} \log_{10}(I_0/I) d\lambda = \frac{e^2}{4\epsilon_0 m_e c^2} N_B d \lambda_0^2 f_{ik} \quad (1)$$

in which: e is the elementary charge, ϵ_0 is the permittivity of vacuum, m_e is the electron mass, c is the speed of light, λ_0 is the absorption wavelength, f_{ik} is the atomic absorption oscillator strength, and d is the measured sample thickness. Actually, since the 2s²3s(²S) ← 2s²2p(²P) and 2s2p(²D) ← 2s²2p(²P) B/pH₂ absorptions overlap, we integrate over both bands simultaneously and replace the term $\lambda_0^2 f_{ik}$ in eqn. (1) with the sum $(\lambda_0^2 f_{ik} + \lambda_0'^2 f_{ik'})$ for the two transitions. We

estimate the number densities of trapped B₂H₆ molecules, N_{B₂H₆}, from the observed IR spectra using an integrated form of Beer's Law:⁷³

$$2.303 \int_{\text{band}} \log_{10}(I_0/I) d\bar{\nu} = \frac{N_{\text{B}_2\text{H}_6}}{N_A} \int_{\text{band}} \alpha_{\text{B}_2\text{H}_6}(\bar{\nu}) d\bar{\nu} \quad (2)$$

in which: N_A is Avogadro's constant, and $\int_{\text{band}} \alpha_{\text{B}_2\text{H}_6}(\bar{\nu}) d\bar{\nu}$ is the integrated vibrational absorption coefficient for the ν_{17} mode. These number densities are normalized by the number density of the pH₂ host at liquid helium temperatures,⁷⁶ and the resulting concentrations reported in units of parts-per-million (PPM).

From the spectra in figures 10 and 11, and using gas-phase values for the various intrinsic atomic⁷⁷ and molecular⁹³ absorption parameters, we estimate the initial concentrations of B atoms and B₂H₆ molecules in the as-deposited sample as ≈ 1 and 3 PPM, respectively; after photobleaching the concentrations are ≈ 0 and 4 PPM, respectively. Keeping in mind the large intrinsic strength of the B₂H₆ ν_{17} transition (integrated absorption coefficient ≈ 650 km/mol)⁹³ and the low dopant concentrations involved, we do not detect any IR absorptions attributable to other reaction products¹⁷ in these photobleaching experiments. The observed 1 PPM growth of B₂H₆ at the expense of only a 1 PPM decrease in B atom concentration suggests either: (a) formation of B₂H₆ via photolysis of another additional (invisible) B containing precursor species, or (b) significant uncertainties in our concentration determinations for the two species. We are in the process of investigating the details of the photochemistry of our B/pH₂ samples, in conjunction with our on-going IR studies.

Figure 12 shows a summary of the B/pH₂ absorption, photobleaching, and emission lineshape data, presented to facilitate comparison with the results of theoretical simulations. The spectra have been converted from distributions in wavelength, $I(\lambda)d\lambda$, to distributions in wavenumber, $I'(\bar{\nu})d\bar{\nu}$, including re-scaling of the intensities by a multiplicative factor of λ^2 (the Jacobian of the $\lambda \rightarrow \bar{\nu}$ transformation). The minor differences between the direct absorption and photobleaching lineshapes give a measure of the experimental uncertainties in these data.

Figure 13 is a schematic depiction of B atom $2s^23s(^2S) \leftrightarrow 2s^22p(^2P)$ photodynamics in B/pH₂ samples. This picture is loosely based on the well established photodynamics of Rydberg transitions of NO molecules trapped in solid pH₂.⁵³⁻⁵⁷ The relative positions of the minima of the B/pH₂ potential energy surfaces are qualitatively correct, as per the known B-H₂ pair potentials and gas-phase spectroscopy.³⁹⁻⁴⁶ The configurational coordinate represents the radial "breathing"

motion of the nearest neighbor pH₂ molecules; the dotted lines are meant to convey the overall confining influence of the pH₂ bulk. The photocycle begins with the trapping cage in the equilibrium geometry appropriate for a ground state B atom. Vertical photo-excitation accesses repulsive regions of the B*/H₂ potential energy surface, resulting in a strongly blue-shifted absorption. The B* excited state survives on a nanosecond timescale, long enough for the nearest neighbor pH₂ molecules to relax away, resulting in nearly un-shifted emission in the enlarged trapping site "bubble."

IV. Conclusions

We assign absorption features observed in the 200 to 250 nm region in spectra of boron doped pH₂, nD₂, Ne, Ar, Kr, and Xe solids to electronic transitions of isolated B atoms. Large gas-to-matrix blue shifts, ranging from +3000 to +7000 cm⁻¹, are observed for the 2s²3s(²S) ← 2s²2p(²P) B atom Rydberg transition. Much smaller shifts are observed for the 2s2p²(²D) ← 2s²2p(²P) B atom core-to-valence transition.

We observe electronic absorptions of B₂ molecules in Rg matrices only. Pairs of peaks spaced by ≈ 10 nm in the 315 to 355 nm region are assigned to the B₂ (A ³Σ_u⁻ ← X ³Σ_g⁻) Douglas-Herzberg transition. A progression of weak peaks in the 260 to 300 nm region is assigned to the B₂ (2) ³Π_u ← X ³Σ_g⁻ transition. We report a novel progression of strong peaks in the VUV region which we suspect are due to B₂ molecules, but which remains unassigned.

We observe trapping of B atoms in nD₂ and pH₂ matrices, but no signs of isolated B₂ molecules. Depositions employing our TASSPI ablation geometry demonstrate that laser ablated B⁺ ions contribute to the yield of trapped B atoms. The peaks at 216.6 and 208.9 nm observed in absorption spectra of B/pH₂ solids are assigned to the matrix perturbed 2s²3s(²S) ← 2s²2p(²P) and 2s2p²(²D) ← 2s²2p(²P) B atom absorptions, respectively. LIF emission spectra of B/pH₂ solids show a single line at 249.6 nm, coincident with the gas phase wavelength of the 2s²3s(²S) → 2s²2p(²P) B atom emission. UV laser irradiation results in photobleaching of the B atom emission and absorptions, accompanied by the formation of B₂H₆. The B atom photobleaching lineshape exactly matches the B atom absorption lineshape.

In B/pH₂ depositions employing laser ablation of solid boron, only about 15 % of the spectroscopically detected boron survives as isolated B atoms, with the remainder reacting to

produce B₂H₆. This suggests that we will require a "milder" source of B atoms if we hope to succeed in increasing the concentrations of isolated B atoms to the ~ 1 % level, and beyond.

Acknowledgments

We gratefully acknowledge numerous helpful conversations with other HEDM program participants over the years. We especially thank the authors of the companion manuscript, Drs. J. Krumrine and S. Jang, and Profs. M. Alexander and G. Voth, as well as Prof. P. Dagdigian, for valuable detailed discussions of B atom spectroscopy in hydrogen clusters and solids. We thank Drs. J. Boatz and J. Sheehy and Prof. P. Langhoff for enlightening discussions concerning computational methods and results, and for their many helpful suggestions. We thank Dr. C.W. Larson for helpful comments concerning our presentation of the concentration determinations.

References

*all journal titles
entire should
be in italics*

1. D.W. Ball, Z.H. Kafafi, L. Fredin, R.H. Hauge, and J.L. Margrave, A Bibliography of Matrix Isolation Spectroscopy: 1954-1985 (Rice U. Press, Houston, TX, 1988).
2. D.W. Ochsner, D.W. Ball, and Z.H. Kafafi, A Bibliography of Matrix Isolation Spectroscopy: 1985-1997 (U.S. Naval Research Laboratory, Washington, DC, 1998).
3. W.R.M. Graham and W. Weltner, Jr., J. Chem. Phys. **65**, 1516 (1976).
4. G.H. Jeong and K.J. Klabunde, J. Am. Chem. Soc. **108**, 7103 (1986).
5. G.H. Jeong, R. Boucher, and K.J. Klabunde, J. Am. Chem. Soc. **112**, 3332 (1990).
6. Y.M. Hamrick, R.J. Van Zee, J.T. Godbout, W. Weltner, Jr., W.J. Lauderdale, J.F. Stanton, and R.J. Bartlett, J. Phys. Chem. **95**, 2840 (1991).
7. Y.M. Hamrick, R.J. Van Zee, and W. Weltner, Jr., J. Chem. Phys. **96**, 1767 (1992).
8. W. Weltner, Jr., R.J. Van Zee, and S. Li, J. Phys. Chem. **99**, 6277 (1995).
9. R.J. Van Zee, A.P. Williams, and W. Weltner, Jr., J. Chem. Phys. **107**, 4756 (1997).
10. L.B. Knight, Jr., B.W. Gregory, S.T. Cobranchi, D. Feller, and E.R. Davidson, J. Am. Chem. Soc. **109**, 3521 (1987).
11. L.B. Knight, Jr., M. Winiski, P. Miller, C.A. Arrington, and D. Feller, J. Chem. Phys. **91**, 4468 (1989).
12. L.B. Knight, Jr., D.W. Hill, T.J. Kirk, and C.A. Arrington, J. Phys. Chem. **96**, 555 (1992).
13. L.B. Knight, Jr., S. Cobranchi, E. Earl, and A.J. McKinley,

- J. Chem. Phys. **105**, 3398 (1996).
14. B.S. Ault, Chem. Phys. Lett. **157**, 547 (1989).
 15. L. Andrews and T.R. Burkholder, J. Phys. Chem. **95**, 8554 (1991).
 16. J.M.L. Martin, P.R. Taylor, J.T. Yustein, T.R. Burkholder, and L. Andrews, J. Chem. Phys. **99**, 12 (1993).
 17. T.J. Tague, Jr. and L. Andrews, J. Am. Chem. Soc. **116**, 4970 (1994).
 18. D.V. Lanzisera, L. Andrews, and P.R. Taylor, J. Phys. Chem. A **101**, 7134 (1997).
 19. J.D. Presilla-Marquez, C.W. Larson, P.G. Carrick, and C.M.L. Rittby, J. Chem. Phys. **105**, 3398 (1996).
 20. J.D. Presilla-Márquez, P.G. Carrick, and C.W. Larson, J. Chem. Phys. **110**, 5702 (1999).
 21. C. W. Larson and J.D. Presilla-Márquez, J. Chem. Phys. **111**, 1988 (1999).
 22. C.W. Larson, J. Harper, and J.D. Presilla-Márquez, Proceedings of the International Union of Pure and Applied Chemistry 10th Symposium on High Temperature Materials Chemistry (April 10-14, 2000 Julich, Germany), K. Hilpert, F.W. Froben, and L. Singheiser, Editors, (Forschungszentrum Julich GmbH, October 2000).
 23. S. Li, R.J. Van Zee, and W. Weltner, Jr., Chem. Phys. Lett. **262**, 298 (1996).
 24. M. Lorenz, J. Agreiter, A.M. Smith, and V.E. Bondybey, J. Chem. Phys. **104**, 3143 (1996).
 25. A.M. Smith, M. Lorenz, J. Agreiter, and V.E. Bondybey, Mol. Phys. **88**, 247 (1996).
 26. J. Agreiter, M. Lorenz, A.M. Smith, and V.E. Bondybey, Chem. Phys. **224**, 301 (1997).
 27. M. Wyss, M. Grutter, and J.P. Maier, J. Phys. Chem. A **102**, 9106 (1998).
 28. M.R. Berman, ed., Proceedings of the High Energy Density Matter (HEDM) Contractors' Conference held 17-20 May 1998 in Monterey, CA (U.S. Air Force Office of Scientific Research, Arlington, VA, 1999).
 29. R.H. Frisbee, "Systems-Level Implications of High Energy Density Matter (HEDM) Propulsion Concepts," in Proceedings of the High Energy Density Matter (HEDM) Contractors' Conference held 12-15 April 1992 in Lancaster, CA, edited by M.R. Berman (U.S. Air Force Office of Scientific Research, Arlington, VA, 1992).
 30. A.T. Pritt, Jr., N. Presser, and R.R. Herm, J. Propulsion and Power **9**, 714 (1993).
 31. R.E. Lo, Aerospace Science and Technology **6**, 359 (1998).
 32. G.P. Sutton, Rocket Propulsion Elements, 6th edition (Wiley, New York, 1992).

33. P.G. Carrick, Specific Impulse Calculations of High Energy Density Solid Cryogenic Rocket Propellants. I. Atoms in Solid H₂, PL-TR-93-3014 (USAF Phillips Laboratory, Edwards AFB, CA, 1993).
34. S.J. Isakowitz, International Reference Guide to Space Launch Systems, (American Institute of Aeronautics and Astronautics, Washington, DC, 1991).
35. M.E. Fajardo, S. Tam, T.L. Thompson, and M.E. Cordonnier, Chem. Phys. **189**, 351 (1994).
36. E. Hwang, Y.L. Huang, P.J. Dagdigian, and M.H. Alexander, J. Chem. Phys. **98**, 8484 (1993).
37. E. Hwang and P.J. Dagdigian, Chem. Phys. Lett. **233**, 483 (1995).
38. X. Yang, E. Hwang, P.J. Dagdigian, M. Yang, and M.H. Alexander, J. Chem. Phys. **103**, 2779 (1995).
39. M.H. Alexander, J. Chem. Phys. **99**, 6014 (1993).
40. M.H. Alexander and M. Yang, J. Chem. Phys. **103**, 7956 (1995).
41. X. Yang, E. Hwang, M.H. Alexander and P.J. Dagdigian, J. Chem. Phys. **103**, 7966 (1995).
42. G. Chaban and M.S. Gordon, J. Phys. Chem. **100**, 95 (1996).
43. C.W. Bauschlicher, Jr., Chem. Phys., Lett. **261**, 637 (1996).
44. P.J. Dagdigian and X. Yang, Faraday Discuss. **108**, 287 (1997).
45. M.S. Gordon, V.A. Glezakou, and D.R. Yarkony, J. Chem. Phys. **108**, 5657 (1998).
46. J. Williams and M.H. Alexander, J. Chem. Phys. **112**, 5722 (2000).
47. J.A. Boatz and M.E. Fajardo, "Monte Carlo Simulations of the Structures and Optical Absorption and Emission Spectra of Na/Ar and B/Ar Solids," in Proceedings of the High Energy Density Matter (HEDM) Contractors' Conference held 6-8 June 1993 in Woods Hole, MA, edited by T.L. Thompson, PL-TR-93-3041, (USAF Phillips Laboratory, Edwards AFB, CA, 1993).
48. M.H. Alexander, A.W. Walton, M. Yang, X. Yang, E. Hwang, and P.J. Dagdigian, J. Chem. Phys. **106**, 6320 (1997).
49. J.R. Krumrine, M.H. Alexander, X. Yang, and P.J. Dagdigian, J. Chem. Phys. **112**, 5037 (2000).
50. A. Vegiri, M.H. Alexander, S. Gregurik, A.B. McCoy, and R.B. Gerber,

- J. Chem. Phys. **101**, 2577 (1994).
51. S. Jang, S. Jang, and G.A. Voth, "Largescale Quantum Computer Simulations of Solid Hydrogen Doped with Lithium and Boron Impurities," in ref. 21.
 52. J.R. Krumrine, S. Jang, G.A. Voth, and M.H. Alexander, J. Chem. Phys. **XXX**, yyy (zzzz); companion article in this journal.
 53. C. Jeannin, M.T. Portella-Oberli, F. Vigliotti, and M. Chergui, Chem. Phys. Lett. **279**, 65 (1997).
 54. F. Vigliotti, M. Chergui, M. Dickgiesser, and N. Schwentner, Faraday Discuss. **108**, 139 (1997).
 55. F. Vigliotti, G. Zerza, M. Chergui, and J. Rubayo-Soneira, J. Chem. Phys. **109**, 3508 (1998).
 56. F. Vigliotti, and M. Chergui, Chem. Phys. Lett. **296**, 316 (1998);
erratum: Chem. Phys. Lett. **305**, 187 (1999).
 57. F. Vigliotti, C. Jeannin, M.T. Portella-Oberli, M. Chergui, and R. Scholz, J. Luminescence **83-43**, 135 (1999).
 58. A.E. Douglas and G. Herzberg, Can. J. Res. **18**, 165 (1940).
 59. H. Bredohl, I. Dubois, and P. Nzohabonayo, J. Mol. Spec. **93**, 281 (1982).
 60. H. Bredohl, I. Dubois, and F. Melen, J. Mol. Spec. **121**, 128 (1987).
 61. C.R. Brazier and P.G. Carrick, J. Chem. Phys. **96**, 8684 (1992).
 62. C.R. Brazier and P.G. Carrick, J. Chem. Phys. **100**, 7928 (1994).
 63. M. Dupuis and B. Liu, J. Chem. Phys. **68**, 2902 (1978).
 64. P.J. Bruna and J.S. Wright, J. Chem. Phys. **91**, 1126 (1989).
 65. S.R. Langhoff and C.W. Bauschlicher, Jr., J. Chem. Phys. **95**, 5882 (1991).
 66. M. Hachey, S.P. Karna, and F. Grien, J. Phys. B **25**, 1119 (1992).
 67. M.R. Manaa and D.R. Yarkony, J. Chem. Phys. **100**, 8204 (1994).
 68. M. Macler and M.E. Fajardo, Mat. Res. Soc. Symp. Proc. **285**, 105 (1993).
 69. M. Macler and M.E. Fajardo, Appl. Phys. Lett. **65**, 159 (1994).
 70. M. Macler and M.E. Fajardo, Appl. Phys. Lett. **65**, 2275 (1994).
 71. M. Macler and M.E. Fajardo, Mat. Res. Soc. Symp. Proc. **388**, 39 (1995).
 72. M.E. Fajardo and M. Macler, U.S. Patent #5,567,935, (1996).
 73. S. Tam, M. Macler, and M.E. Fajardo, J. Chem. Phys. **106**, 8955 (1997).

74. M.E. Fajardo and S. Tam, J. Chem. Phys. **108**, 4237 (1998).
75. S. Tam and M.E. Fajardo, Rev. Sci. Instrum. **70**, 1926 (1999).
76. I.F. Silvera, Rev. Mod. Phys. **52**, 393 (1980).
77. W.L. Wiese, M.W. Smith, and B.M. Glennon, Atomic Transition Probabilities Vol. I, (NSRDS-NBS-4, 1966).
78. G.W. Bethke, J. Chem. Phys. **31**, 669 (1959).
79. E. Merzbacher, Quantum Mechanics, (Wiley, New York, 1970).
80. W.E. Baylis, J. Phys. B **10**, L477 (1977).
81. L.C. Balling and J.J. Wright, J. Chem. Phys. **79**, 2941 (1983).
82. P.W. Langhoff, J. Phys. Chem. **100**, 2974 (1996).
83. J.A. Boatz, unpublished results.
84. C. Steinbruchel and D.M. Gruen, J. Chem. Phys. **74**, 205 (1981).
85. D.C. Silverman and M.E. Fajardo, J. Chem. Phys. **106**, 8964 (1997).
86. S.A. Ruatta, L. Hanley, and S.L. Anderson, J. Chem. Phys. **91**, 226 (1989).
87. J. Nichols, M. Gutowski, S.J. Cole, and J. Simons, J. Phys. Chem. **96**, 644 (1992).
88. M. Gutowski, M. Roberson, J. Rusko, J. Nichols, and J. Simons, J. Chem. Phys. **99**, 2601 (1993).
89. Weast, R.C., ed., CRC Handbook of Chemistry and Physics, 60th edition, (CRC Press, Boca Raton, 1980).
90. J.L. Duncan, J. Harper, E. Hamilton, and G.D. Nivellini, J. Mol. Spec. **102**, 416 (1983).
91. R.L. Sams, T.A. Blake, S.W. Sharpe, J.M. Flaud, and W.J. Lafferty, J. Mol. Spec. **191**, 331 (1998).
92. W.L. Wiese and G.A. Martin, "Atomic Spectroscopy," in A Physicist's Desk Reference, H.L. Anderson, editor (American Institute of Physics, New York, 1989).
93. M. Shen and H.F. Schaefer III, J. Chem. Phys. **96**, 2968 (1992).

Tables:

Table I. Electronic absorptions of B atoms isolated in as-deposited (as-dep.) and annealed matrices. Shown are vacuum wavelengths (nm), wavenumbers (cm^{-1}), and gas-to-matrix shifts $\Delta E_{\text{gm}}(\text{cm}^{-1}) = E_{\text{matrix}} - E_{\text{gas}}$. Gas phase data from ref. [77].

matrix	$2s2p^2(^2D) \leftarrow 2s^22p(^2P)$			$2s^23s(^2S) \leftarrow 2s^22p(^2P)$		
	$\lambda_{\text{vac}}(\text{nm})$	$\bar{\nu}(\text{cm}^{-1})$	$\Delta E_{\text{gm}}(\text{cm}^{-1})$	$\lambda_{\text{vac}}(\text{nm})$	$\bar{\nu}(\text{cm}^{-1})$	$\Delta E_{\text{gm}}(\text{cm}^{-1})$
gas phase	208.96	47856	NA	249.75	40040	NA
pH ₂	208.9	47870	+10	216.6	46170	+6130
nD ₂ , as dep.	204?	49000	+1100	207? 214*?	48300 46700	+8260 +6700
Ne, as dep.	205.4* 207.4	48690 48220	+830 +360	215.4	46430	+6390
Ne, annealed	207.4	48220	+360	216.0	46300	+6260
Ar, as dep.	208.4	47980	+120	213.9 223.0*?	46750 44840	+6710 +4800
Ar, annealed	208.5	47960	+100	214.0	46730	+6690
Kr, as dep.	210.3	47550	-310	226.7 235.8*?	44110 42400	+4070 +2360
Xe, as dep.	211.9 219.8*?	47190 45500	-670 -2350	231.9 252.6*?	43120 39590	+3080 -450

NA - not applicable.

* - secondary trapping site.

? - tentative assignment.

Table II. Douglas-Herzberg ((2) $^3\Sigma_u^- \leftarrow X\ ^3\Sigma_g^-$) absorptions of B₂ molecules isolated in as-deposited (as-dep.) and annealed matrices. Shown are the vibrational assignments, vacuum wavelengths (nm), wavenumbers (cm⁻¹), and gas-to-matrix shifts $\Delta E_{gm}(\text{cm}^{-1}) = E_{\text{matrix}} - E_{\text{gas}}$; $\Delta G_{1/2}(\text{cm}^{-1})$ is the first vibrational separation in the upper state. Gas phase data from ref. [59]. The gas phase averages are calculated assuming natural isotopic abundance ratio of $^{10}\text{B}:^{11}\text{B} = 1:4$, and hence $^{10}\text{B}^{11}\text{B}:^{11}\text{B}_2 = 1:2$.

matrix	band	$\lambda_{\text{vac}}(\text{nm})$	$\bar{\nu}(\text{cm}^{-1})$	$\Delta E_{gm}(\text{cm}^{-1})$	$\Delta G_{1/2}(\text{cm}^{-1})$
gas phase $^{10}\text{B}^{11}\text{B}$	1-0		31472.1	NA	954.5
	0-0		30517.6		
gas phase $^{11}\text{B}_2$	1-0		31450.6	NA	932.2
	0-0		30518.4		
gas phase average	1-0		31458	NA	940
	0-0		30518		
Ne, as dep.	1-0	317.2	31530	+70	950*
		317.8	31470	+10	
	0-0	327.0	30580	+60	
		327.6	30520	0	
Ne, annealed	1-0	317.2	31530	+70	950*
		327.0	30580	+60	
	0-0	327.3	30550	+30	
		327.8	30510	-10	
Ar, annealed	1-0	320.4	31210	-250	950
	0-0	330.5	30260	-260	
Kr, as dep.	1-0	324.4	30830	-630	960
	0-0	334.8	29870	-650	
Xe, as dep.	1-0	332.2	30100	-1360	950
	0-0	343.1	29150	-1370	

NA - not applicable.

* - $\Delta G_{1/2}$ calculated from similar features in each band; see lineshapes in Fig. 3.

Table III. Summary of available experimental (expt.) and theoretical (theo.) spectroscopic constants of the ground $^3\Sigma_g^-$, and excited $^3\Sigma_u^-$ and $^3\Pi_u$ states of $^{11}\text{B}_2$.

state	R_e (Å)	T_e (cm $^{-1}$)	ω_e (cm $^{-1}$)	source
$X\ ^3\Sigma_g^-$	1.590	0	1051.3	DH (1940), expt.
	1.622	0	989	DL (1978), theo.
	1.590	0	1052.7	BDN (1982), expt.
	1.594	0	1058	BW (1989), theo.
	1.600	0	1041	LB (1991), theo.
	1.595	0	1064	HKG (1992), theo.
(1) $^3\Pi_u$	1.744	3300	816	BW (1989), theo.
	1.764	3380	806	LB (1991), theo.
	1.734	3470	848	HKG (1992), theo.
	1.744		818.00	BC (1994), expt.
(1) $^3\Sigma_u^-$	1.565	14829	1104	DL (1978), theo.
	1.544	14415	1188	LB (1991), theo.
	1.545	15200	1189	HKG (1992), theo.
(2) $^3\Sigma_u^-$	1.625	30573	937.4	DH (1940), expt.
	1.660	31438	885	DL (1978), theo.
	1.625	30574.4	937.2	BDN (1982), expt.
	1.647	31091	926	LB (1991), theo.
	1.599	30000	965	HKG (1992), theo.
(2) $^3\Pi_u$	1.465	34600	1346	BW (1989), theo.
	1.471	34875	1322	LB (1991), theo.
	1.478	34500	1318	HKG (1992), theo.
	1.458			BC (1992), expt.
(3) $^3\Pi_u$	1.725	44769	1116	LB (1991), theo.
	1.744	43800	1020	HKG (1992), theo.

DH (1940) - ref. 58.

DL (1978) - ref. 63.

BDN (1982) - ref. 59.

BW (1989) - ref. 64.

LB (1991) - ref. 65.

HKG (1992) - ref. 66.

BC (1992) - ref. 61.

BC (1994) - ref. 62.

Table IV. Proposed $(2) {}^3\Pi_u \leftarrow X {}^3\Sigma_g^-$ absorptions of B_2 molecules isolated in as-deposited matrices. Shown are the tentative vibrational assignments, vacuum wavelengths (nm), and wavenumbers (cm^{-1}); $\Delta G_{v+1/2}$ (cm^{-1}) is the difference between adjacent lines in each vibrational progression.

matrix	band	λ_{vac} (nm)	$\bar{\nu}$ (cm^{-1})	$\Delta G_{v+1/2}$ (cm^{-1})
Ne	3-0	264.2	37850	1290
	2-0	273.5	36560	1340
	1-0	283.9	35220	1340
	0-0	295.2	33880	
Ar	3-0	266.1	37580	1350
	2-0	276.0	36230	1330
	1-0	286.5	34900	1320
	0-0	297.8	33580	
Kr, prog. #1	4-0	259.3	38570	1330
	3-0	268.5	37240	1290
	2-0	278.2	35950	1360
	1-0	289.1	34590	1370
	0-0	301.1	33220	
Kr, prog. #2	3-0	265.4	37680	1360
	2-0	275.3	36320	1280
	1-0	285.4	35040	1370
	0-0	297.0	33670	

Table V. Unassigned VUV absorptions in as-deposited B/Rg matrices. Shown are vacuum wavelengths (nm), and wavenumbers (cm^{-1}); $\Delta G_{v+1/2}$ (cm^{-1}) is the difference between adjacent lines in the apparent vibrational progression.

matrix	λ_{vac} (nm)	$\bar{\nu}$ (cm^{-1})	$\Delta G_{v+1/2}$ (cm^{-1})
Ne, prog. #1	180.2	55490	
	183.3	54560	930
	186.6	53590	970
Ne, prog. #2	181.4	55130	
	184.6	54170	960
	187.9	53220	950
Ar	179	55870	
	182	54950	920
	185.5	53910	1040
	188.8	52970	940
	192.4	51980	990
Kr	184.6	54170	
	187.7	53280	890
	191.1	52330	950
	194.5	51410	920
	198.4	50400	1010

Figure Captions:

FIG. 1. Experimental Diagrams.

FIG. 2. Survey optical absorption spectra of (a) B/Ne, (b) B/Ar, (c) B/Kr, and (d) B/Xe matrices; instrumental resolution ≈ 1.2 nm FWHM. The triangles indicate the wavelengths of a few well-known gas-phase B atom and B₂ molecular transitions. All four depositions employ the CLOSE geometry using a focused XeCl ablation laser ($\lambda_{\text{abl}} = 308$ nm) operating at a repetition rate of 5 Hz. Trace (a) is for a 3 μ thick B/Ne sample at $T = 5$ K, as deposited under the following conditions: ablation intensity $\Phi_{\text{abl}} \sim 3 \times 10^8$ W/cm², pulse energy = 15 mJ/pulse, deposition time $t_{\text{dep}} = 10$ min, Ne flow rate $F_{\text{Ne}} = 1.1$ mmol/hr; the absorbance is scaled by a multiplicative factor of 2. Trace (b) is for a 6 μ thick B/Ar sample at $T = 10$ K, as deposited using: $\Phi_{\text{abl}} \sim 5 \times 10^8$ W/cm², 27 mJ/pulse, $t_{\text{dep}} = 10$ min, $F_{\text{Ar}} = 1.2$ mmol/hr. Trace (c) is for a 14 μ thick B/Kr sample at $T = 20$ K, as deposited using: $\Phi_{\text{abl}} \sim 4 \times 10^8$ W/cm², 20 mJ/pulse, $t_{\text{dep}} = 20$ min, $F_{\text{Kr}} = 1.3$ mmol/hr; we correct for optical scattering by the Kr host by subtracting the absorbance spectrum of a 13 μ thick pure Kr sample. Trace (d) is for a 4 μ thick B/Xe sample at $T = 30$ K, as deposited using: $\Phi_{\text{abl}} \approx 7 \times 10^8$ W/cm², 30 mJ/pulse, $t_{\text{dep}} = 10$ min, $F_{\text{Xe}} = 0.6$ mmol/hr; we correct for optical scattering by the Xe host by subtracting the absorbance spectrum of an 8 μ thick pure Xe sample.

FIG. 3. Optical absorption spectra of (a) B/Ne, (b) B/10% nD_2 /Ne matrices, and (c) Schumann-Runge bands of O₂ in laboratory air; instrumental resolution ≈ 0.3 nm FWHM, no correction is made for optical scattering by the matrix hosts. Both matrix depositions employ the CLOSE geometry using a focused XeCl ablation laser ($\lambda_{\text{abl}} = 308$ nm) operating at a repetition rate of 5 Hz. Trace (a) is for a 1.7 μ thick B/Ne sample at $T = 4.5$ K, as deposited under the following conditions: $\Phi_{\text{abl}} \sim 3 \times 10^8$ W/cm², 11 mJ/pulse, $t_{\text{dep}} = 10$ min, $F_{\text{Ne}} = 1.4$ mmol/hr. Trace (b) is for a 1.2 μ thick B/10% nD_2 /Ne sample at $T = 4$ K, as deposited under the following conditions: $\Phi_{\text{abl}} \sim 3 \times 10^8$ W/cm², 10 mJ/pulse, $t_{\text{dep}} = 10$ min, $F_{\text{Ne}} = 1.2$ mmol/hr.

FIG. 4. Optical absorption spectra obtained during annealing of a B/Ne sample; instrumental resolution ≈ 0.3 nm FWHM, no correction is made for optical scattering by the Ne host. The

peaks in the 200 to 220 nm region are due to isolated B atoms. Trace (a) is for the 3 μ thick B/Ne sample at $T = 5$ K, as deposited in CLOSE geometry using: $\lambda_{abl} = 308$ nm, rep. rate = 5 Hz, $\Phi_{abl} \sim 2 \times 10^8$ W/cm², 8 mJ/pulse, $t_{dep} = 10$ min, $F_{Ne} = 1.5$ mmol/hr. Trace (b) shows the spectrum at $T = 7$ K, trace (c) at $T = 10$ K, and trace (d) upon cooling to $T = 5$ K.

FIG. 5. Optical absorption spectra obtained during annealing of a B/Ne sample; instrumental resolution ≈ 0.3 nm FWHM, no correction is made for optical scattering by the Ne host. The peaks near 318 and 327 nm are due to the B_2 ($A^3\Sigma_u^- \leftarrow X^3\Sigma_g^-$) Douglas-Herzberg transition. Trace (a) is for the 12 μ thick B/Ne sample at $T = 5$ K, as deposited in CLOSE geometry using: $\lambda_{abl} = 308$ nm, rep. rate = 5 Hz, $\Phi_{abl} \sim 2 \times 10^8$ W/cm², 8 mJ/pulse, $t_{dep} = 30$ min, $F_{Ne} = 1.3$ mmol/hr. Trace (b) shows the spectrum at $T = 7$ K, trace (c) at $T = 10$ K, trace (d) upon cooling to $T = 5$ K, trace (e) at $T = 12$ K, and trace (f) upon re-cooling to $T = 5$ K.

FIG. 6. Optical absorption spectra obtained during annealing of a B/Ar sample; instrumental resolution ≈ 0.3 nm FWHM, no correction is made for optical scattering by the Ar host. The peaks in the 180 to 195 nm region are tentatively assigned to B_2 molecules, the peaks in the 200 to 220 nm region are due to isolated B atoms. Trace (a) is for the 3 μ thick B/Ar sample at $T = 10$ K, as deposited in CLOSE geometry using: $\lambda_{abl} = 308$ nm, rep. rate = 5 Hz, $\Phi_{abl} \sim 5 \times 10^8$ W/cm², 27 mJ/pulse, $t_{dep} = 10$ min, $F_{Ar} = 0.7$ mmol/hr. Trace (b) shows the spectrum at $T = 35$ K, and trace (c) upon cooling to $T = 10$ K. The oscillations in the baseline are thin-film transmission interference fringes. The inset shows a correlation plot of the integrated intensities of the 208.4 and 213.9 nm peaks, including data from 37 spectra of 5 different samples. The straight line fit has a slope of 1.25, and a correlation coefficient of 0.969.

FIG. 7. Optical absorption spectra obtained during annealing of a B/nD₂ sample; instrumental resolution ≈ 0.3 nm FWHM, no correction is made for optical scattering by the nD₂ host. The feature near 205 nm is due to isolated B atoms. Trace (a) is for the 7 μ thick B/nD₂ sample at $T = 3.5$ K, as deposited in CLOSE geometry using: $\lambda_{abl} = 308$ nm, rep. rate = 5 Hz, $\Phi_{abl} \sim 2 \times 10^8$ W/cm², 8 mJ/pulse, $t_{dep} = 10$ min, $F_{nD_2} = 1.4$ mmol/hr. Trace (b) shows the spectrum at $T = 6.2$

K, and trace (c) upon cooling to $T = 3.5$ K. The oscillations in the baseline are thin-film transmission interference fringes.

FIG. 8. Optical absorption spectra of two different as-deposited B/pH₂ samples; instrumental resolution ≈ 0.3 nm FWHM, no correction is made for optical scattering by the pH₂ host. The peaks at 209 and 217 nm are due to isolated B atoms; the concentrations of isolated B atoms are between 0.1 and 1 PPM. Both depositions employ the TASSPI ablation geometry using a focused XeCl ablation laser ($\lambda_{abl} = 308$ nm) operating at a repetition rate of 10 Hz. Trace (a) is for a 2.3 mm thick B/pH₂ sample at $T = 2.4$ K, as deposited using: $\Phi_{abl} \approx 6 \times 10^8$ W/cm², 100 mJ/pulse, $t_{dep} = 60$ min, $F_{pH_2} = 129$ mmol/hr; the ion-rejection magnets are absent. Trace (b) is for a 2.2 mm thick B/pH₂ sample at $T = 2.4$ K, as deposited using: $\Phi_{abl} \approx 6 \times 10^8$ W/cm² (105) - more to not
line to be
of unit

FIG. 9. Laser induced fluorescence spectrum of B atoms in a B/pH₂ sample at $T = 2.4$ K; instrumental resolution ≈ 0.3 nm FWHM. The unfocused dye laser excitation beam is ≈ 3 mm in diameter; wavelength is 217.0 nm, 120 μ J/pulse, pulse duration ≈ 20 ns. The emission is integrated over a 1 μ s wide window, with the excitation pulse occurring within the first 100 ns; the spectrum is the sum of 100 events. The 0.6 mm thick B/pH₂ sample is deposited in CLOSE geometry using: $\lambda_{abl} = 308$ nm, rep. rate = 5 Hz, $\Phi_{abl} \approx 8 \times 10^8$ W/cm², 21 mJ/pulse, $t_{dep} = 15$ min, $F_{pH_2} = 146$ mmol/hr. The triangle shows the position of the gas phase B atom line.

FIG. 10. Photobleaching of the B atom absorptions in a B/pH₂ sample; instrumental resolution ≈ 1.2 nm FWHM. The B/pH₂ sample is the same as depicted above in FIG. 9. Trace (a) is the optical absorption spectrum of the as-deposited B/pH₂ sample at $T = 2.4$ K, trace (b) shows the spectrum following irradiation by ≈ 1000 pulses of the excitation laser with $\lambda_{exc} = 210$ and 220 nm, and trace (c) is the difference (a)-(b).

FIG. 11. IR absorption spectra of the ν_{17} band region of B₂H₆. The sample is the same as depicted above in FIGS. 9 and 10. Trace (a) is for the as-deposited B/pH₂ sample at $T = 2.4$ K,

trace (b) shows the spectrum following irradiation by ≈ 1000 pulses of the excitation laser with $\lambda_{\text{exc}} = 210$ and 220 nm.

FIG. 12. Comparison of absorption (solid trace), photobleaching (dotted trace), and emission (dashed trace) lineshapes in B/pH₂. The absorption and photobleaching spectra are shifted vertically to give 0 absorbance at 40000 cm^{-1} , then rescaled vertically to give 1.0 absorbance at the peak near 48000 cm^{-1} .

FIG. 13. Qualitative schematic of B atom $2s^23s(^2S) \leftrightarrow 2s^22p(^2P)$ photodynamics in B/pH₂ samples.

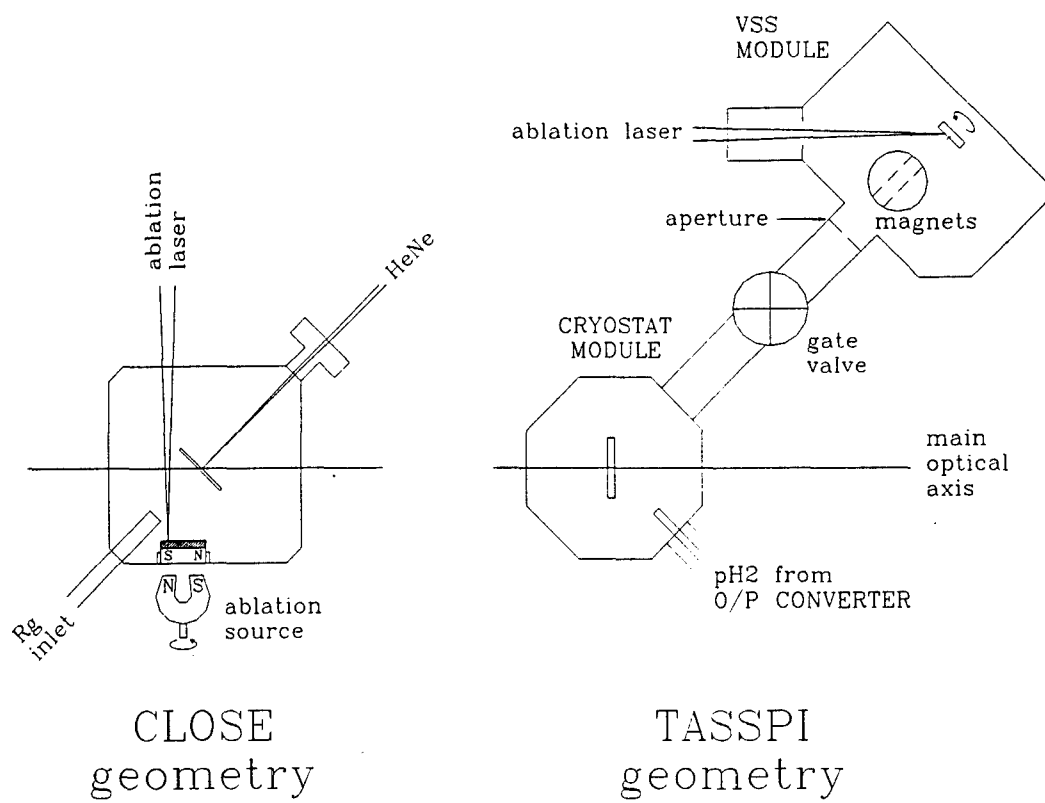


FIG. 1. Experimental Diagrams.

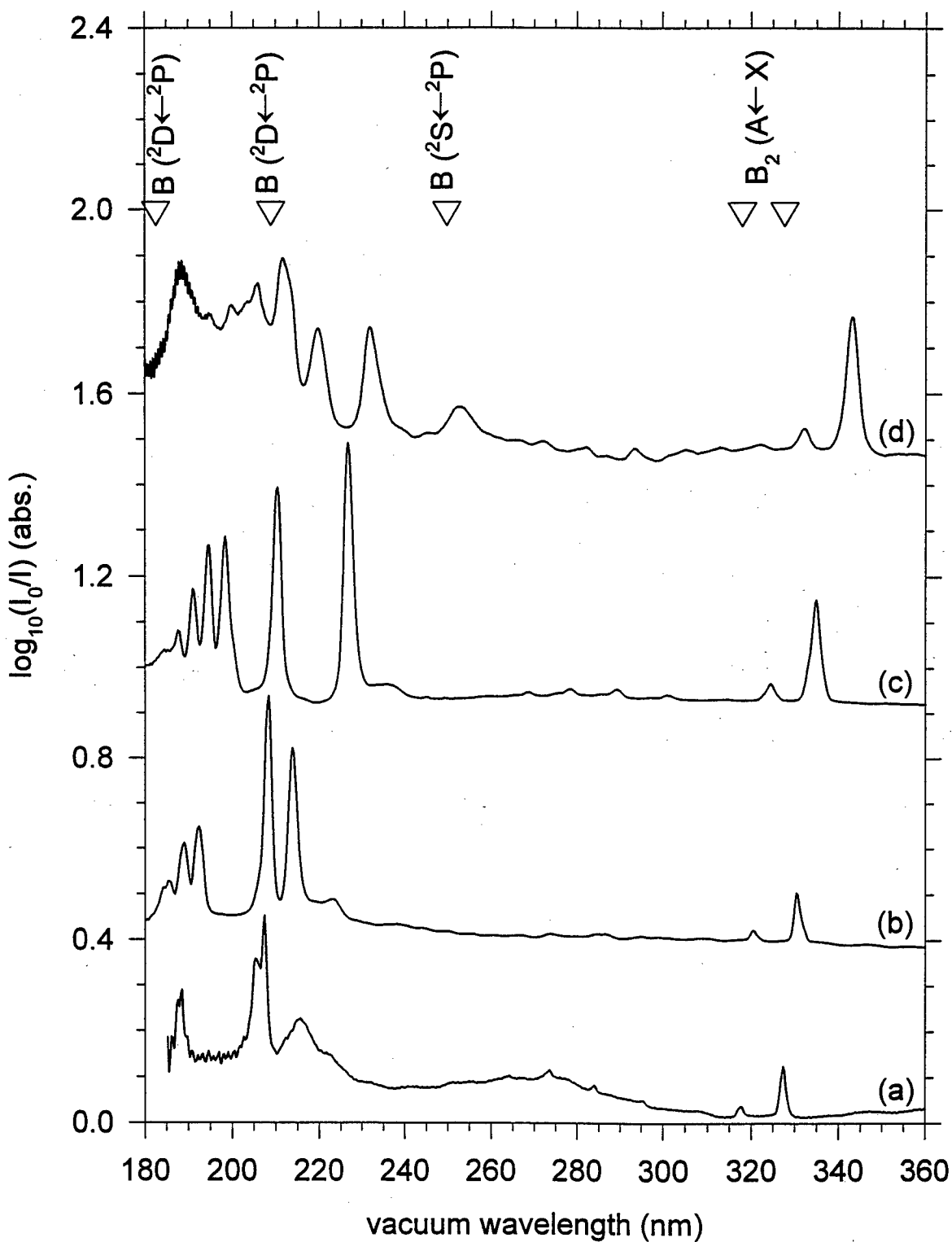


FIG. 2. Survey optical absorption spectra of (a) B/Ne, (b) B/Ar, (c) B/Kr, and (d) B/Xe matrices.

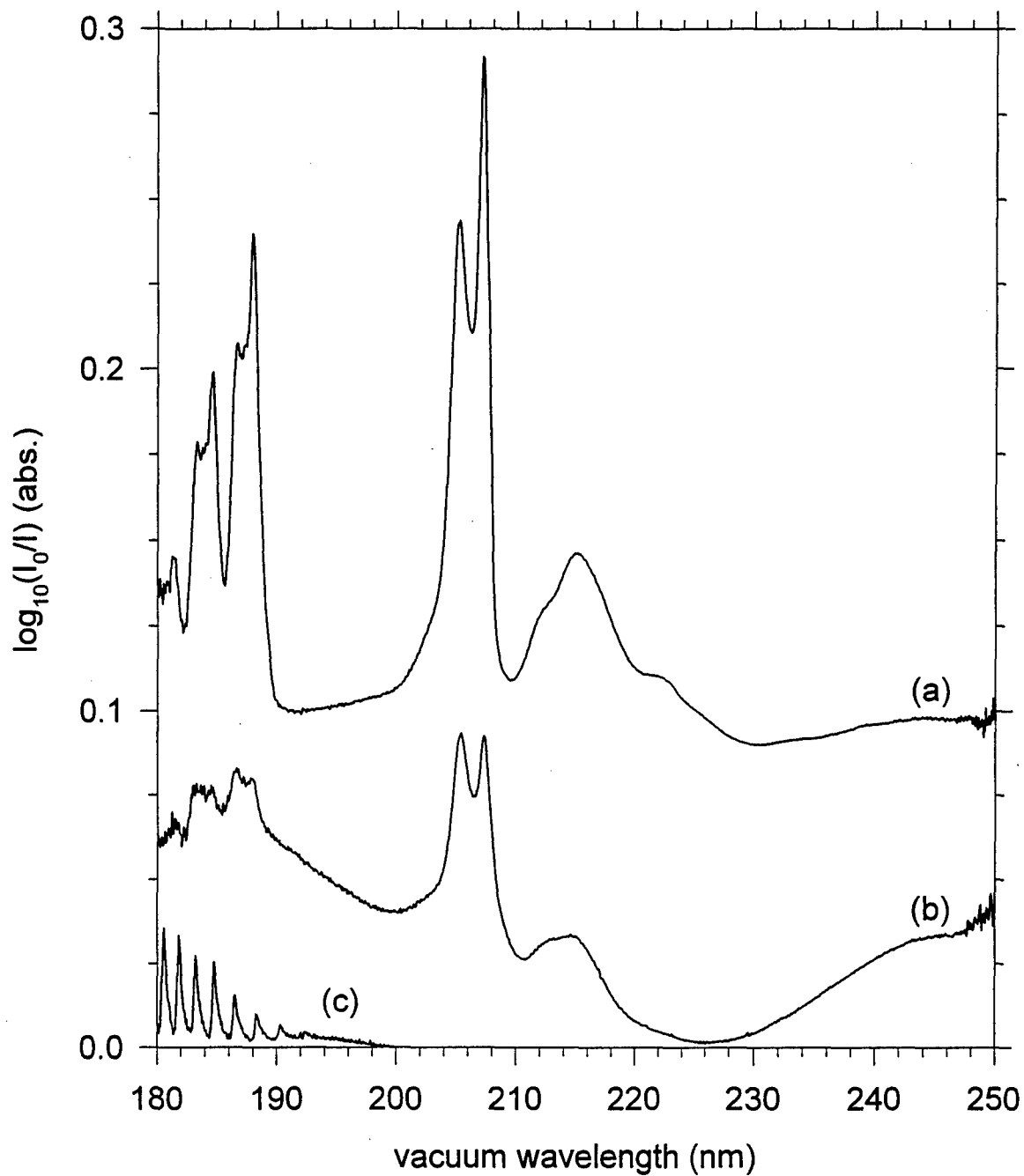


FIG. 3. Optical absorption spectra of (a) B/Ne, (b) B/10% n D₂/Ne matrices, and (c) Schumann-Runge bands of O₂ in laboratory air.

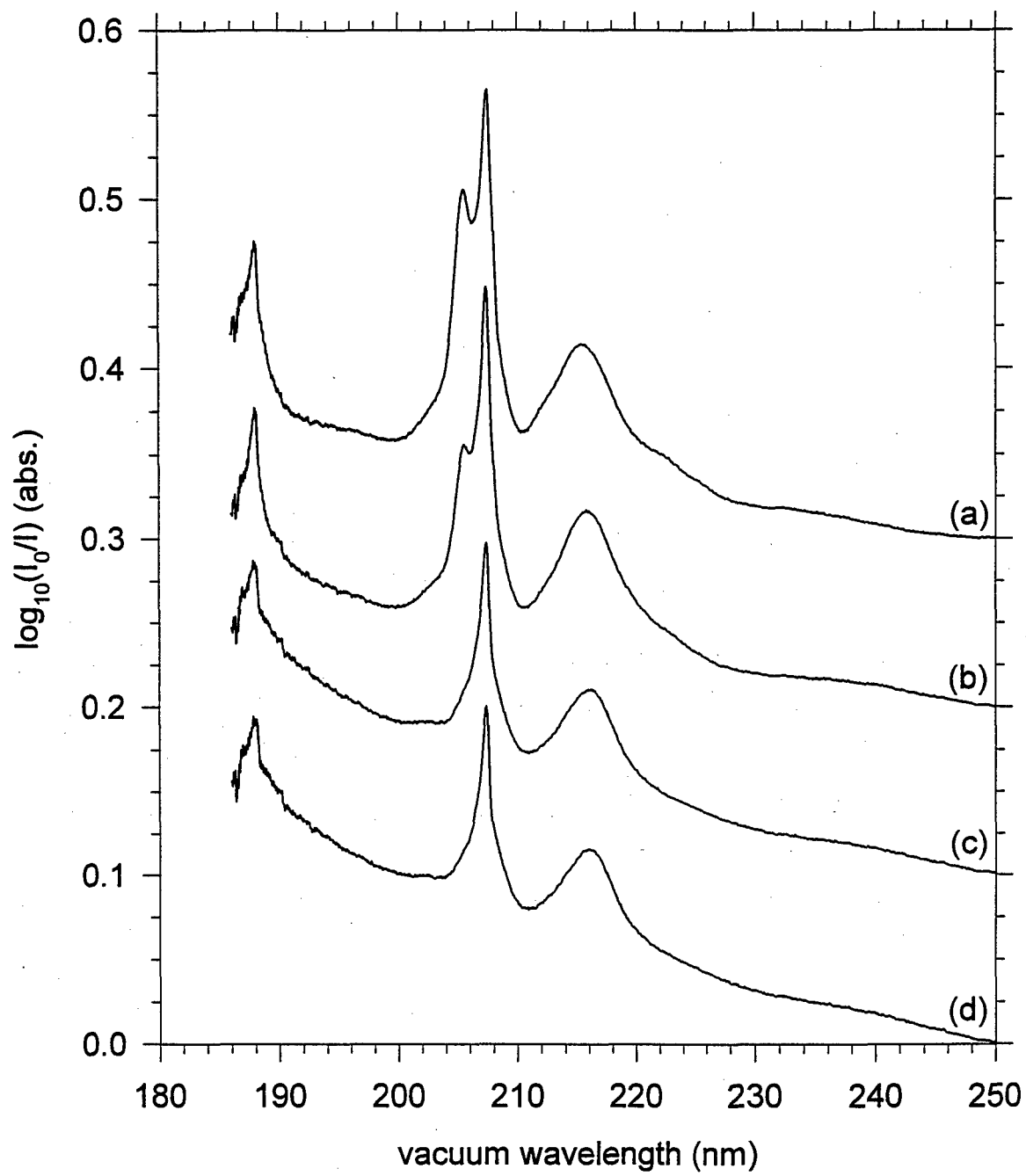


FIG. 4. Optical absorption spectra obtained during annealing of a B/Ne sample.

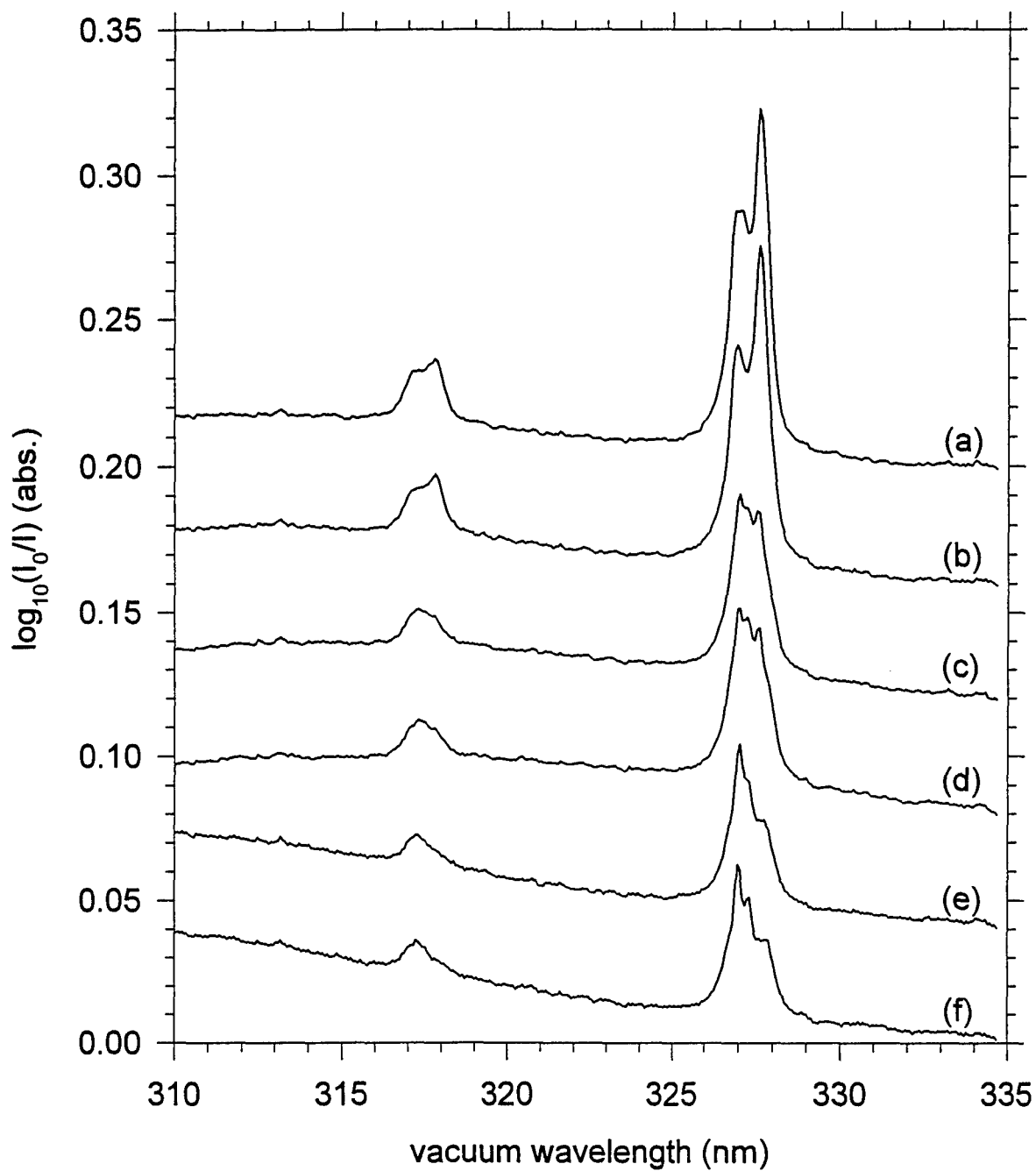


FIG. 5. Optical absorption spectra obtained during annealing of a B/Ne sample.

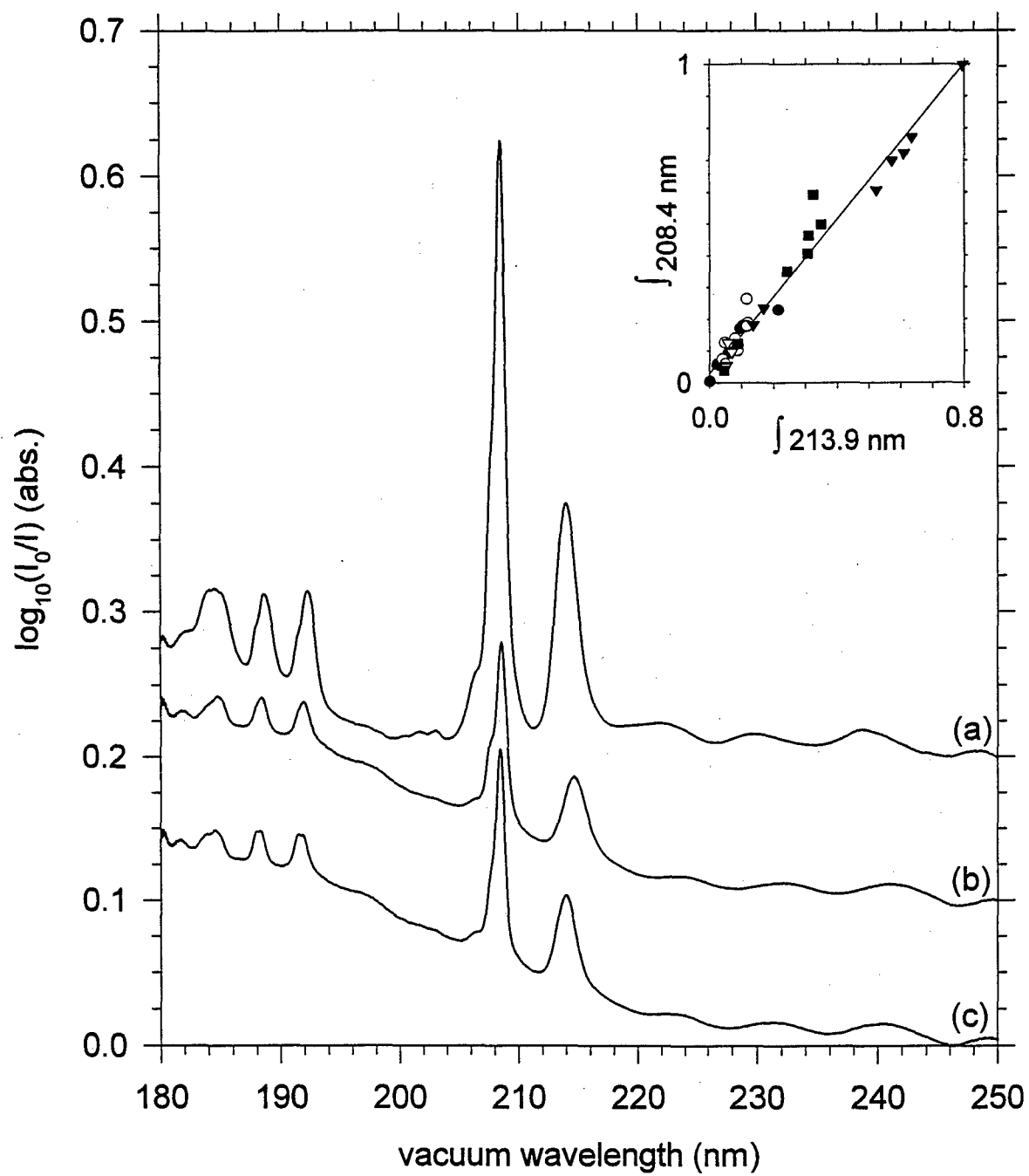


FIG. 6. Optical absorption spectra obtained during annealing of a B/Ar sample.

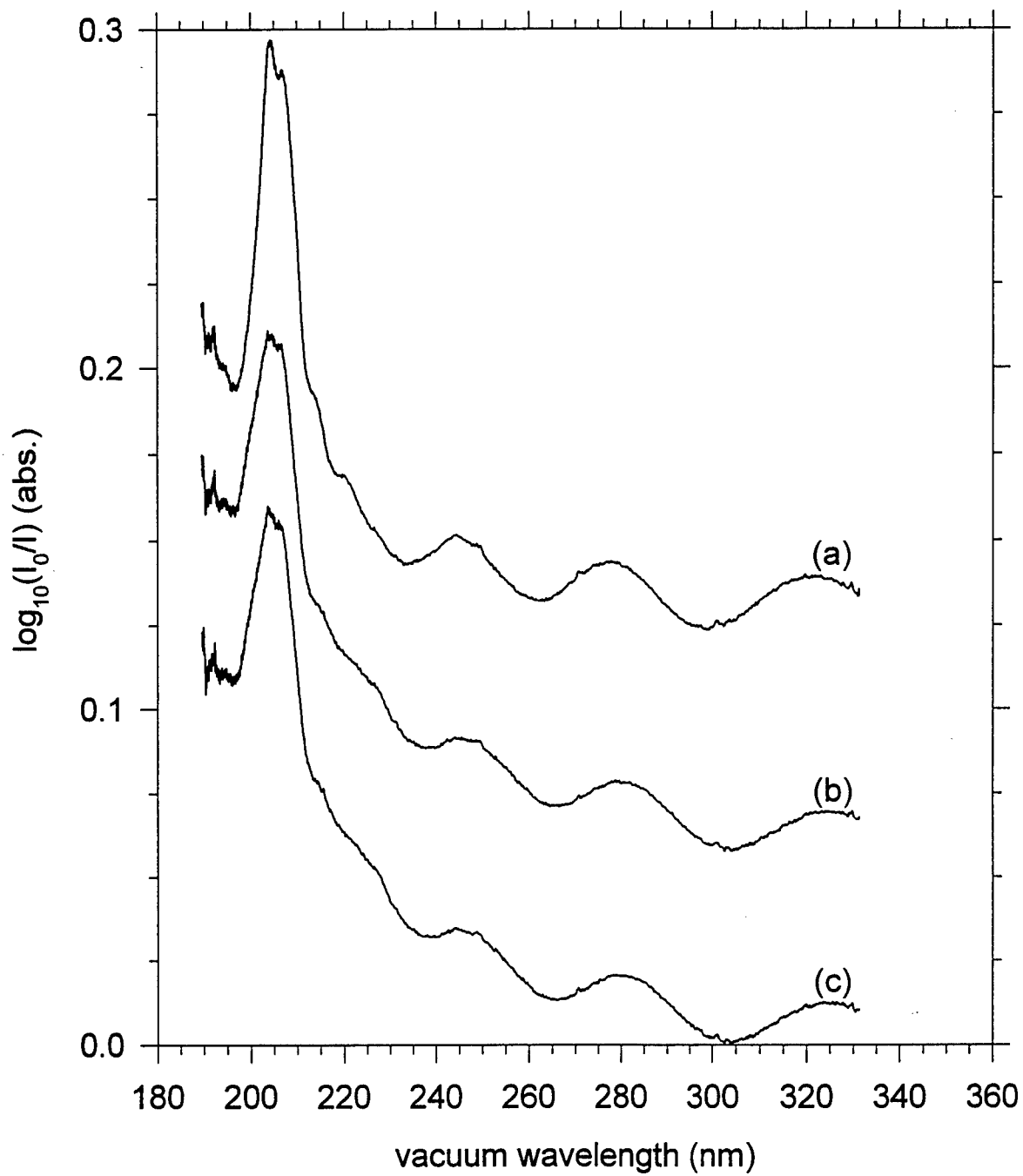


FIG. 7. Optical absorption spectra obtained during annealing of a B/nD₂ sample.

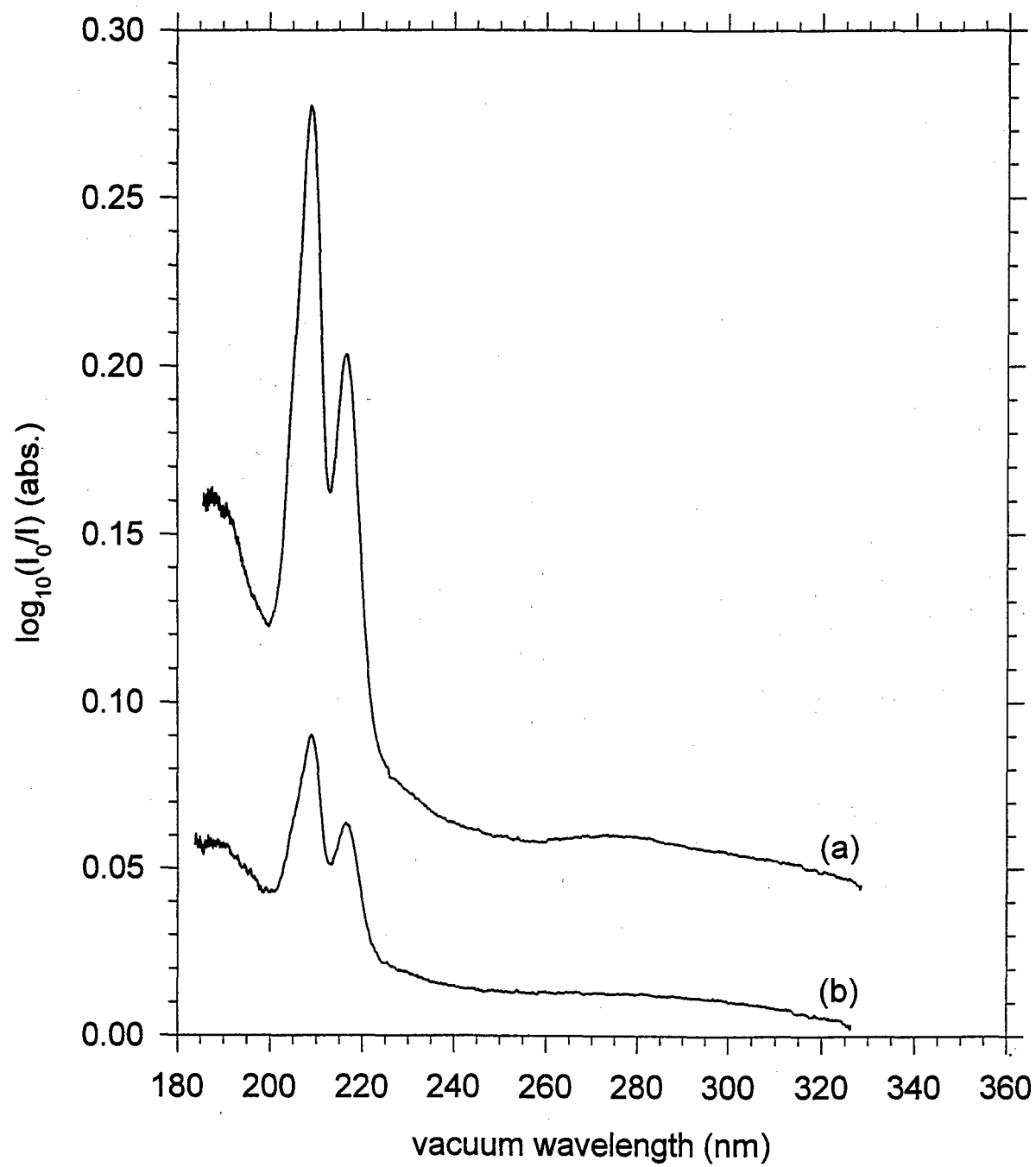


FIG. 8. Optical absorption spectra of two different as-deposited B/pH₂ samples.

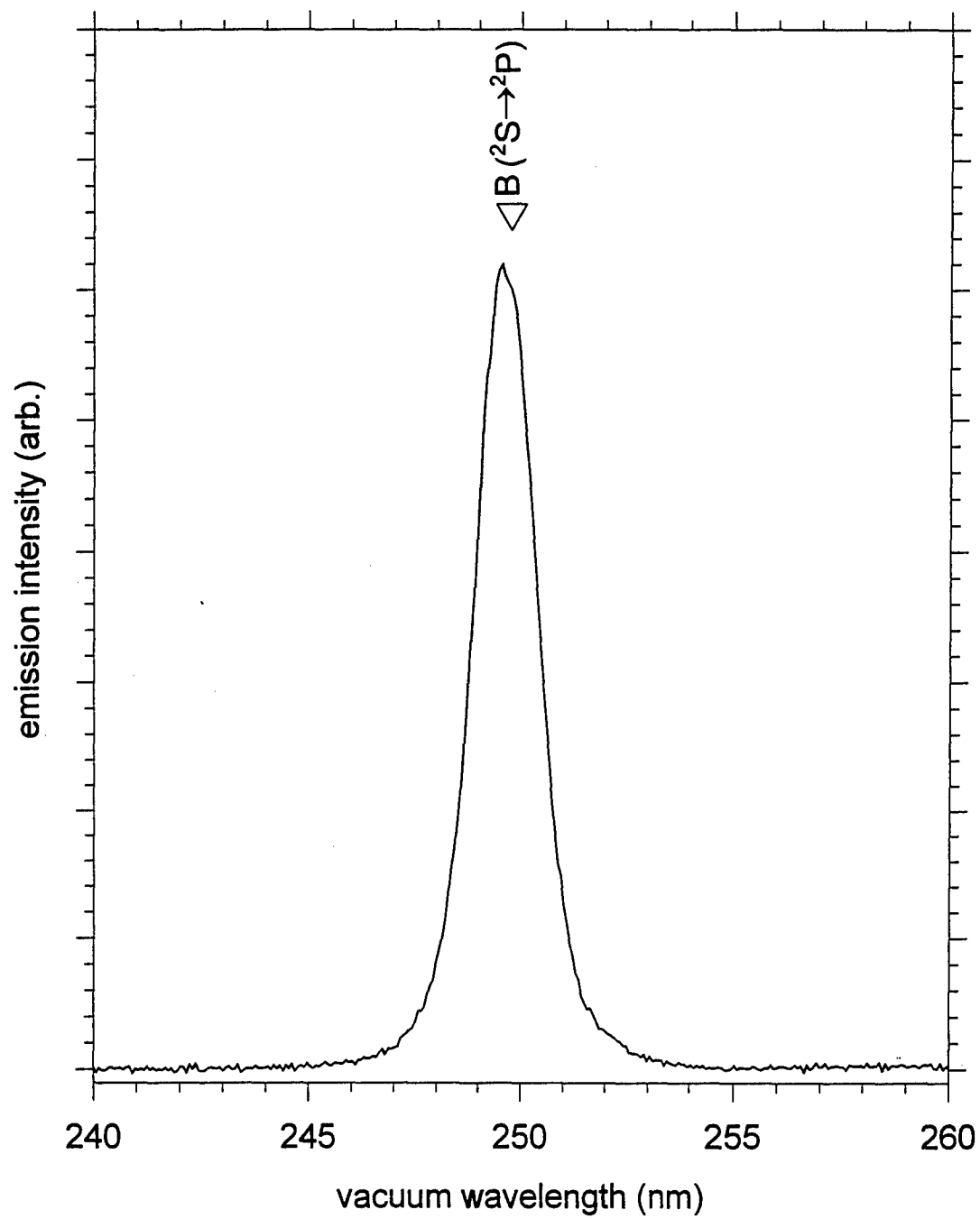


FIG. 9. Laser induced fluorescence spectrum of B atoms in a B/pH₂ sample at T = 2.4 K.

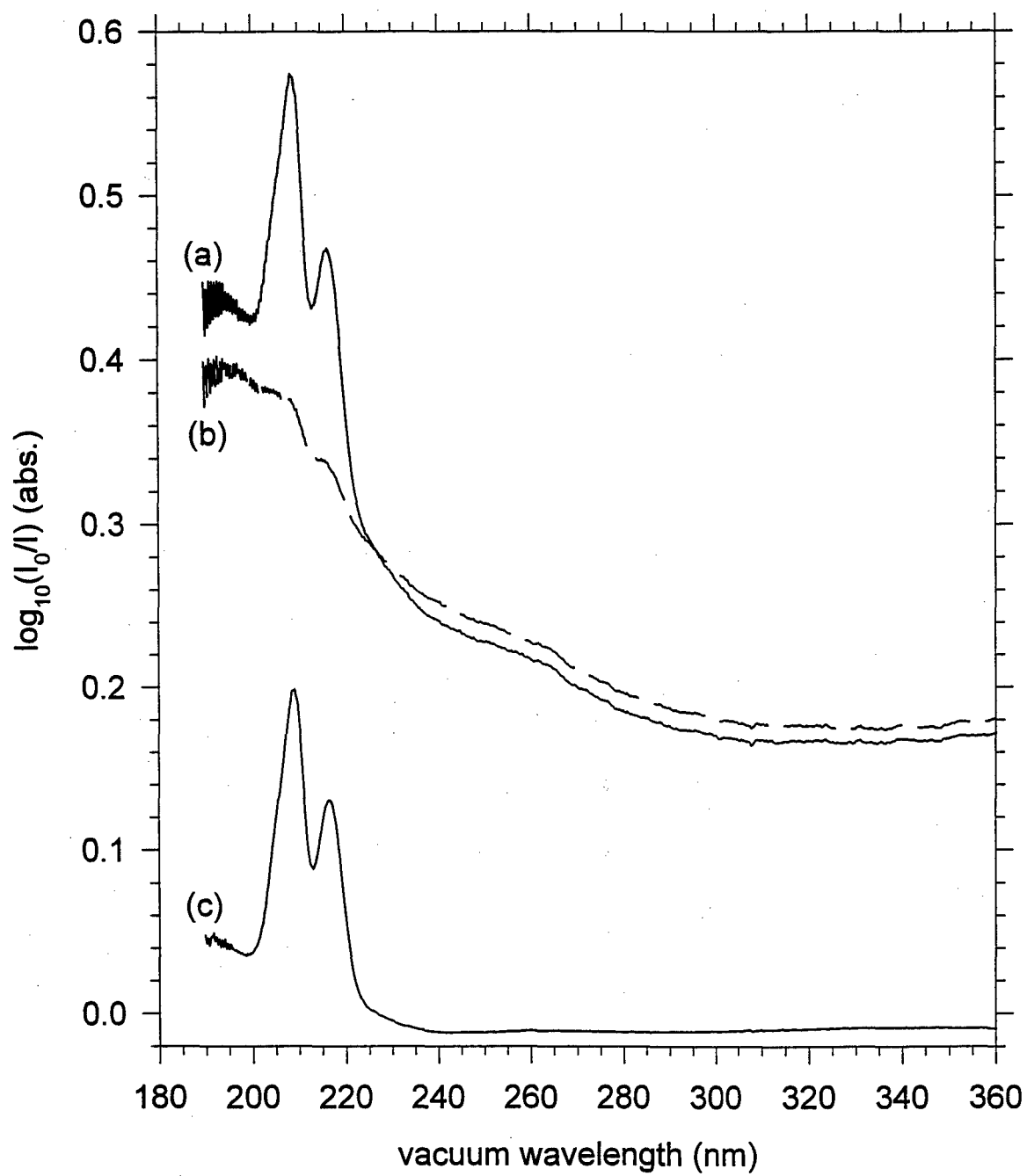


FIG. 10. Photobleaching of the B atom absorptions in a B/pH₂ sample.

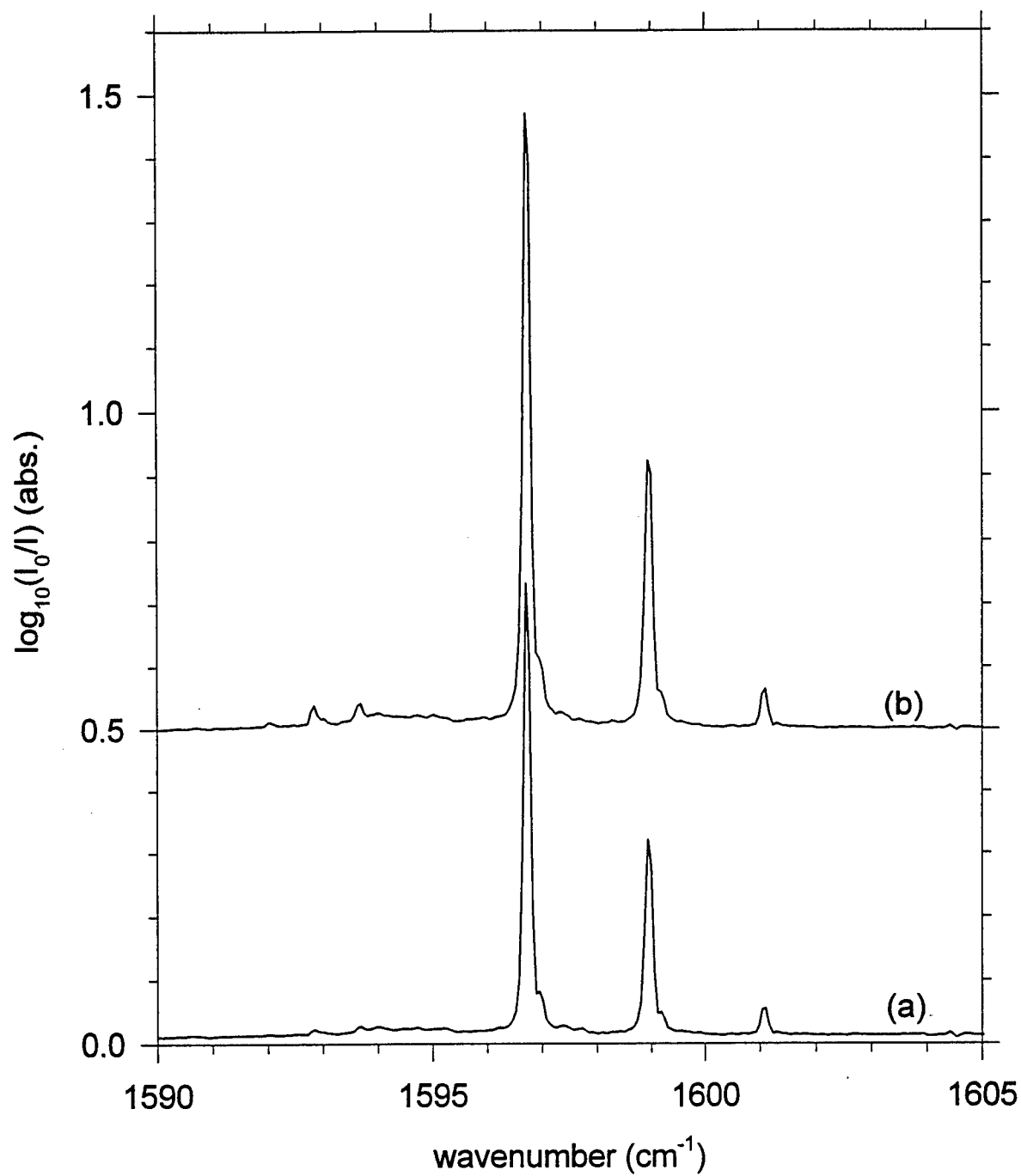


FIG. 11. IR absorption spectra of the ν_{17} band region of B_2H_6 .

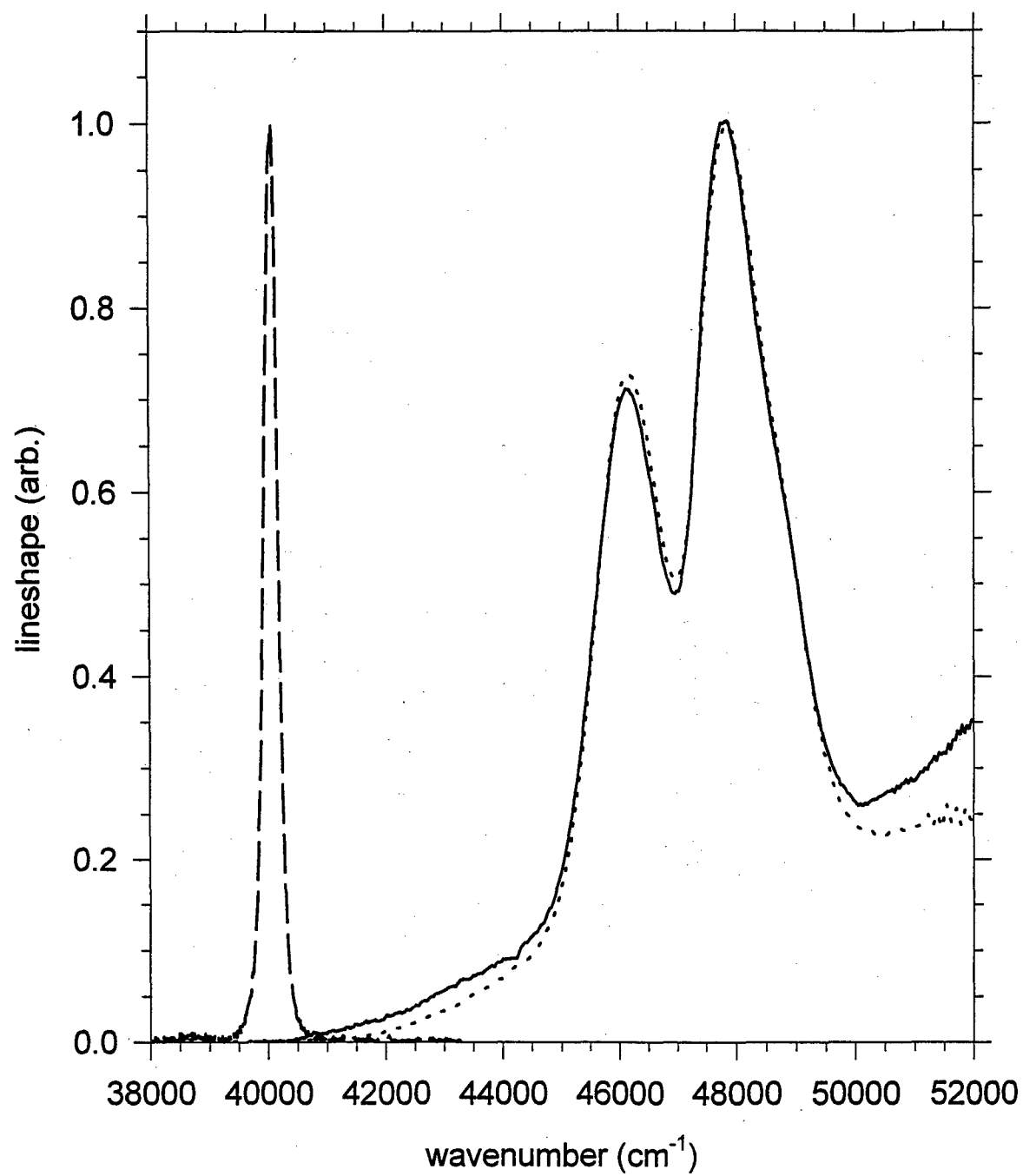


FIG. 12. Comparison of absorption, photobleaching, and emission lineshapes in B/pH₂.

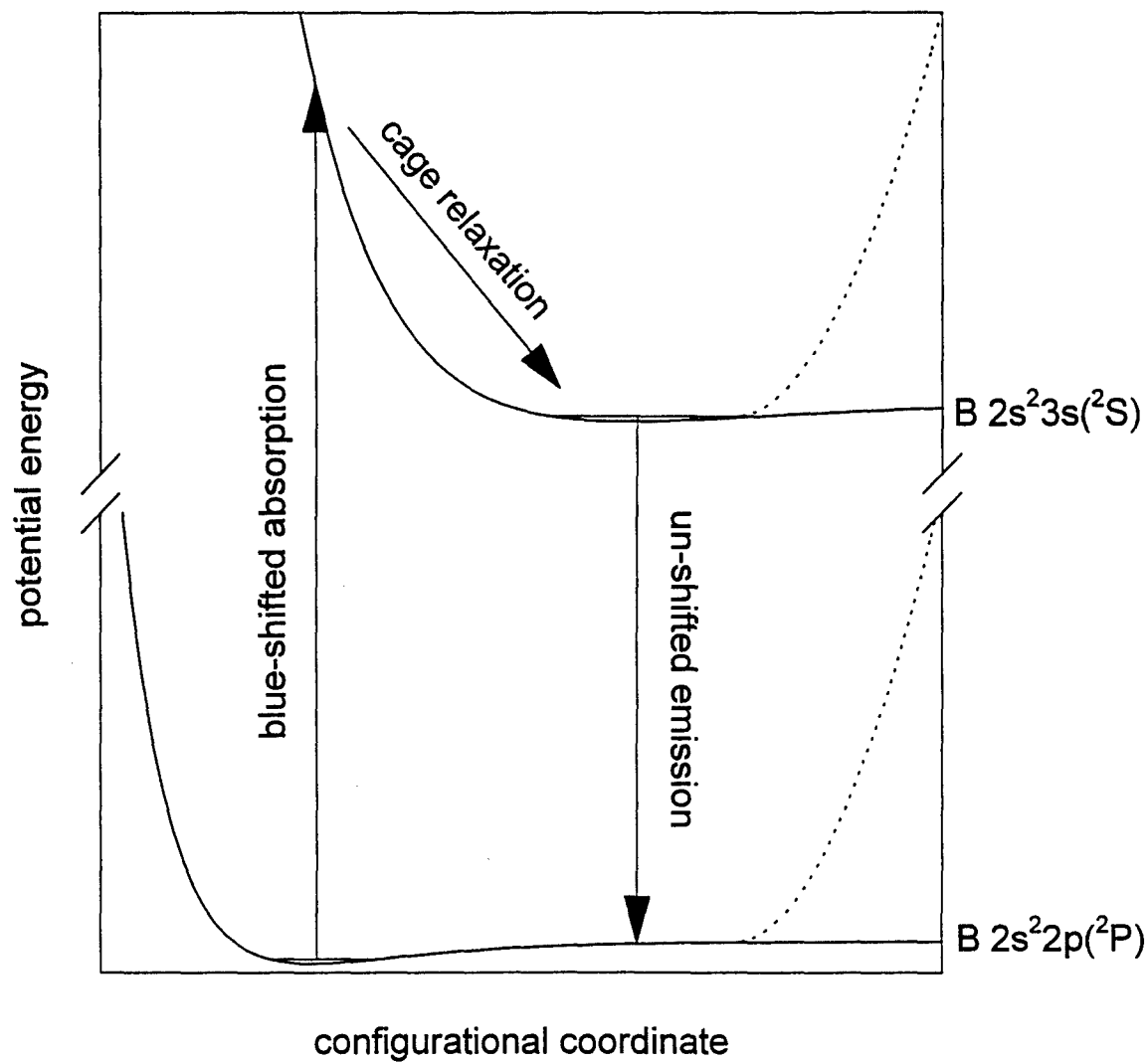


FIG. 13. Qualitative schematic of B atom $2s^23s(^2S) \leftrightarrow 2s^22p(^2P)$ photodynamics in B/pH₂ samples.